THESIS

ARSENIC DOPING, KINETIC BEHAVIOR AND OXIDE FORMATION FOR POLYCRYSTALLINE CdTe THIN FILMS PHOTOVOLTAICS

Submitted by

Mayank N. Mate

Department of Mechanical Engineering

In partial fulfillment of the requirements

For the Degree of Master of Science

Colorado State University

Fort Collins, Colorado

Summer 2024

Master's Committee:

Advisor: Walajabad Sampath

Co-Advisor: Amit Munshi

James Sites

Copyright by Mayank N. Mate 2024

All Rights Reserved

ABSTRACT

ARSENIC DOPING, KINETIC BEHAVIOR, AND OXIDE FORMATION FOR POLYCRYSTALLINE CdTe THIN-FILM PHOTOVOLTAICS

CdTe thin-film photovoltaics (PV) is one of the most promising renewable energy technologies currently in the market. Since the inception of CdTe PV in the 1950s, the technology has come a long way to be one of the most efficient solar cell technologies on the planet.

However, there are still challenges associated with this technology which limit the power conversion efficiency. Currently, the most efficient CdTe solar cell to have been fabricated is still only at ~69% of the maximum possible efficiency, given by the Shockley-Queisser (SQ) limit. Performance loss analysis has suggested that the limiting electrical parameter is the open-circuit voltage (V_{oc}) and detailed investigations have suggested that a defect state within the bandgap of Se allowed CdTe contributes significantly to this loss of V_{oc}, which can be observed by Photoluminescence (PL).

For thin-film CdTe PV to realize its full potential, research has been ongoing to improve the V_{oc} by doping CdTe with a group V dopant, as well as passivating the surface of CdTe which causes significant recombination of charged carriers and may inhibit voltage even further.

The research in this thesis focuses on group-V doping using As as the dopant and Cd_3As_2 as the doping material, and the formation of TeO_2 as the metal oxide on the surface of CdTe. The goal of this research was to observe any improvements in V_{oc} and overall device performance with As doping, TeO_2, and a combination of both, and whether As doping mitigates the primary defect state within the bandgap of Se alloyed CdTe.

To investigate the effects of these doping and surface treatments, three key hypotheses statements were formed.

The first hypothesis is that As can be incorporated into CdTe using Cd_3As_2 without depositing it as a separate layer. This distinction of not depositing a film of Cd_3As_2 is important, and it aims to avoid any complexes caused by depositing Cd_3As_2 on the CdTe surface, creating another interface and potentially limiting the device performance, particularly due to Cd_3As_2 being a semi-metal. Secondary-Ion Mass Spectroscopy (SIMS) and X-Ray Photoelectron Spectroscopy (XPS) were used as the characterization methods to confirm the incorporation of As into the CdTe film by dissociation and diffusion, without depositing a layer of Cd_3As_2.

The second hypothesis is that exposing a CdTe film to ambient air at high temperatures can lead to the enhanced formation of TeO_2. Metal oxides such as Al_2O_3 have long been investigated to passivate the surface of CdTe, improving carrier lifetime and Voc. Traditionally, these metal oxides have been sputtered onto the surface, while native oxides on the surface of CdTe take a long time to form, on the timescale of days to weeks. However, this hypothesis investigates a novel method of forming a native layer of TeO_2 by annealing a CdTe film in vacuum at elevated temperatures (~500℃) and rapidly exposing it to atmospheric oxygen while the high temperature is maintained. XPS and PL characterization was performed on the films that had undergone this ‘rapid oxidation’, and the formation of TeO_2 was confirmed. The effect of TeO_2 was combined with As doping, as well as compared in an undoped film, and it demonstrated a significant improvement in V_{oc} when compared to control samples that were Cu doped and undoped with no intentional formation of TeO_2.

The third and final hypothesis is that As doping using Cd_3As_2 mitigates the sub-band-gap emission in photoluminescence originating from Se alloyed CdTe. To confirm or deny this theory, absolute PL was measured with an InGaAs detector, for samples that were doped with As and for

samples that had a combination As doping treatments and/or TeO_2 formed by using the method described for hypothesis two. The photoluminescence results showed no mitigation of the sub-band-gap emission in Se alloyed CdTe films that were doped with As. However, the addition of TeO_2 demonstrated a lowering of the sub-bandgap emission intensity and overall improvement to the band-gap PL emission.

Additionally, electrical parameters of six distinct device structures were measured and compared, with Cu-doped and undoped Se-alloyed CdTe being the reference/control samples. As a result of this research, a cell measuring close to 18% power conversion efficiency was measured with As doping, the native TeO_2 layer, and one third of the Cu doping that went into reference samples. Finally, this research also provides some insight into the effects of high O_2 presence during the As doping process using Cd_3As_2, and how it inhibits the ionization of As a small P-type dopant.

ACKNOWLEDGEMENTS

Firstly, I would like to thank my committee for the time, effort, and guidance they invested in making this project a possibility. I want to thank Dr. Sites, whose instructions and advice have been so comprehensive and made me a better public speaker, and for helping collaborate with NREL, which was a critical step in progressing my research. To Dr. Sampath and Dr. Munshi, who have my immense gratitude for trusting me with this project, supporting and advising me, and sharing their passion for renewable energy. I have learned more from them than I ever imagined. They have pushed me to think critically, ask more questions than to chase answers, work hard, and to be an effective, ethical scientist.

To my mother and father, who raised me and shaped me into the person I am today. Their lessons of morals, patience, kindness, and resilience will always be invaluable. My Father is a businessman and engineer who works in renewable energy. Since my childhood, my father used to tell me about his experiences in graduate school, and the work he did for his doctorate degree, which has been my inspiration to pursue knowledge at the graduate level and beyond. To my mother, who is an artist through and through, and motivates me to combine the best of both worlds, in my personal, and academic life. And to both, to push me beyond my comfort zone, and making me learn things that can only be taught from experience.

My thanks to the researchers and professors at CSU, who have trained me on sophisticated characterization tools and opened a door to further knowledge and learning.

A heartfelt thanks to my lab mates and fellow students at the PV lab, who have worked hard to do effective, meaningful research, that has supplemented my own. Thank you all for your help and support. A special thanks to Sushmakanth. You have given me so many ideas and helped me achieve this. You are a person that is very easy to talk to, be it research, or anything else. I will always appreciate our arguments, discussions, and your politeness to laugh at the worst of my jokes. To Daniel, thank you for

lending your skills and setting up the InGaAs detector at the physics laboratory and helping me take measurements. It was a crucial step to making progress toward this thesis.

Thank you to all the funding agencies, the NSF, the DOE, and the I/UCRC for your financial support and oversight.

My family and friends, advisors, lab mates, collaborators, and teachers made it all possible for me to be where I am today. Thank you all.

TABLE OF CONTENTS

ABSTRACT ii
ACKNOWLEDGEMENTS v
LIST OF FIGURES ix
Chapter 1: INTRODUCTION 1
1.1 Climate Change and the Need for Renewable Energy 1
1.2 Understanding Materials: 4
1.3 What is the P-N junction and how does a solar cell work? 8
1.4 What is CdTe and CdSeTe? 9
1.5 CdTe research at the Center of Advanced Photovoltaics 11
1.6 Understanding the limit of CdTe solar cell performance. 12
Chapter 2: LITERATURE REVIEW 14
2.2 Limitations of Copper Doping 15
2.3 P-type doping in monocrystalline/MBE grown CdTe PV devices 17
2.4 Group V doping in polycrystalline CdTe PV devices 19
2.5 Oxide Deposition/Formation and passivation 21
Chapter 3: FABRICATION AND CHARACTERIZATION METHODS 26
3.1 Introduction 26
3.2 Superstrate glass information 26
3.3 Window layer deposition 26
3.4 CdSexTe1-x and CdTe deposition 28
3.5 Doping processes 30
3.6 Electrical characterization: 31
    3.6.1 J-V 31
    3.6.2 C-V 33
    3.6.3 Steady State Photoluminescence: 34
3.7 Physical Characterization 34
    3.7.1 Secondary Ion Mass Spectroscopy (SIMS): 34
    3.7.2 X-ray Photoelectron Spectroscopy (XPS) 36
Chapter 4: HYPOTHESIS 1 39
4.1 Background to hypothesis 1 39
4.2 Device fabrication and analysis for hypothesis 1 39

4.2.1 Device fabrication for SIMS analysis 39
4.2.2 SIMS Analysis 41
4.2.3 Device fabrication for XPS analysis 42
4.2.4 XPS analysis 43
4.2 Diffusion of As in $CdSe_xTe_{1-x}$ 45
Chapter 5: HYPOTHESIS 2 48
5.1 Background to Hypothesis 2 48
5.2 Device fabrication and structure for hypothesis 2 49
5.3 XPS analysis of samples for hypothesis 2 50
5.4 Photoluminescence of CdTe with TeO_2 formed by novel method. 53
5.5 Electrical characterization of devices with various doping treatments and TeO_2 54
Chapter 6: HYPOTHESIS 3 57
6.1 Background to hypothesis 3 57
6.2 Device Structure 57
6.3 Photoluminescence measurement 58
6.3.1 Photoluminescence of As doped samples 59
6.3.2 Photoluminescence of reference samples 59
6.3.3 Photoluminescence of an undoped sample with TeO_2 60
Chapter 7: DISCUSSION 62
7.1 J-V parameters of As doped samples without TeO_2 62
7.2 J-V parameters of As doped samples with TeO_2 63
7.3 J-V parameters of As doped samples with TeO_2 with mild Cu doping 64
7.4 J-V parameters of undoped samples with TeO_2 65
7.5 J-V parameters of CSU's baseline samples 66
7.5.1 Cu doped bilayer samples 67
7.5.2 Undoped bilayer samples without TeO_2 68
7.6 C-V Characterization 68
Chapter 8: CONCLUSIONS AND FUTURE WORKS 72
8.1 Summary of results 72
8.2 Future works 72
References 74
APPENDIX A – PUBLICATIONS 77

LIST OF FIGURES

Figure 1 Global Total Greenhouse gas emissions, Land use, land use change (LULUCF) and Fossil Fuel Industry (FFI), [1]. 1

Figure 2 Change in average surface temperature, blue bars= cooler than average, red bars= warmer than average, from [2]. 2

Figure 3 Mass change rate of glaciers, from [3]. 2

Figure 4 Total installed capacity of all renewable technologies and prediction till 2030, [4] 3

Figure 5 The periodic table of elements, from [7] 4

Figure 6 Illustration of the bandgap in materials, from [8]. 6

Figure 7 Illustration of doping in a Si semiconductor, from [9]. 7

Figure 8 Illustration of bandgap in a PN junction; left: P-doped, right: N-doped, from [10]. 9

Figure 9 Structure of the baseline CdTe thin film photovoltaic device at CSU. 11

Figure 10 Carrier concentration vs depletion width of Cu doped and undoped CdTe cells, from [14]. 15

Figure 11 Device structure and band diagram of ASU's 1V V_{oc} CdTe device, from [23]. 17

Figure 12 carrier lifetime in the bulk of MBE grown CdTe vs hole density, with P doping, [24]. 18

Figure 13 Carrier concentration vs Dopant concentration in px-CdTe samples, [26]. 19

Figure 14 Electrical characteristics of px-CdTe devices with various dopants, [27]. 19

Figure 15 TRPL emission spectra of Heterostructures with Al_2O_3, [39]. 22

Figure 16 HAADF STEM image of TeO_2 on a CdTe surface. 23

Figure 17 EELS spectra of Te and O showing a double peak and confirming presence of TeO_2, [35]. 24

Figure 18 Picture of the RF sputtering system for MZO deposition. 27

Figure 19 Top: Picture of the ARDS; Bottom: Picture of the CSS sources inside the ARDS. 28

Figure 20 A picture of the CSS vacuum system for CuCl treatment. 30

Figure 21 Top: Illustration of a J-V curve under light and dark bias; Bottom: Power density curve acquired from the J-V curve. From [38]. 32

Figure 22 Picture of the J-V measurement setup. 33

Figure 23 Picture of the XPS system at CSU. 36

Figure 24 Device structure for SIMS analysis. 40

Figure 25 Concentration profile of As as a function of film depth following the Cd_3As_2 treatment in the HBJ. 41

Figure 26 Left: film structure for reference sample (sample no. 1); right: film structure of Cd_3As_2 treated bilayer (sample no. 2). 43

Figure 27 As 3d photoelectron spectra from reference sample (sample no. 1) 44

Figure 28 As 2p photoelectron spectra from bilayer sample annealed over Cd_3As_2 (sample no. 2) 45

Figure 29 Fitted diffusion models for Cu (left) and As (right) as a function of film depth and time. 46

Figure 30 J-V curves and device parameters of As doped CdTe devices with two doping pathways and sputtered TeOX, by Zachary Lustig, [29]. 48

Figure 31 Film architecture; left: control sample exposed to ambient air at room temperature, right: sample exposed to ambient air at high temperature post Cd_3As_2 treatment in the HBJ. 50

Figure 32 XPS spectra of (a) Te 3d and (b) O 1s spectra in sample where TeO2 was formed at ambient conditions. 51

Figure 33 XPS spectra of (a) Te 3d and (b) O 1s spectra in sample where TeO2 was formed by exposing sample to ambient air at high temperature. 52

Figure 34 Film structure for Photoluminescence measurements. 53

Figure 35 Photoluminescence of Cu doped, As doped, As doped with TeO2 and undoped samples. 54

Figure 36 J-V curves of best performing cells with film architecture shown in figure 33. 55

Figure 37 J-V curve of 18% efficient cell. 55

Figure 38 Various film architectures to investigate emission in photoluminescence of sub-bandgap defects. 58

Figure 39 Absolute Photoluminescence of sub-bandgap and bandgap for As doped bilayer samples with and without TeO_2. 59

Figure 40 Photoluminescence of sub-bandgap and bandgap in Cu doped and undoped bilayer samples. 60

Figure 41 Photoluminescence of sub-bandgap and bandgap emissions in a sample with no intentional doping and TeO_2 by rapid oxidation. 61

Figure 42 J-V parameters of As doped samples without TeO2. 62

Figure 43 J-V parameters of As doped bilayer samples with TeO_2 by rapid oxidation. 63

Figure 44 J-V parameters of As doped samples with TeO_2 and mild Cu doping to improve current. 64

Figure 45 J-V parameters of an undoped bilayer sample with TeO_2. 65

Figure 46 J-V curve of the best performing cell in the undoped bilayer sample with TeO_2. 66

Figure 47 J-V parameters of Cu doped bilayer baseline samples. 67

Figure 48 J-V parameters of undoped bilayer samples. 68

Figure 49 Net hole concentration vs depletion width of bilayer cells. Legend (right) indicates doping and surface treatment. 69

Figure 50 Net hole concentration vs depletion width of bilayer samples with As doping performed in the ARDS, Cu doping performed in the CuCl sublimation system, and an undoped cell. Data from Akash Shah. 70

Chapter 1: INTRODUCTION

1.1 Climate Change and the Need for Renewable Energy

Climate change is the phenomenon observed by the rise in the global average temperature due to the increased presence of greenhouse gases such as CO_2, methane, carbon monoxide, etc. in the atmosphere. These greenhouse gases prevent the heat absorbed by the earth from the sun from being transmitted back into space, causing the rise in global average temperatures. Reliance on combustible fuels such as coal, petroleum oils, and natural gas for energy generation has been pivotal in industrialization and socio-economic modernization. However, relying on these natural but polluting

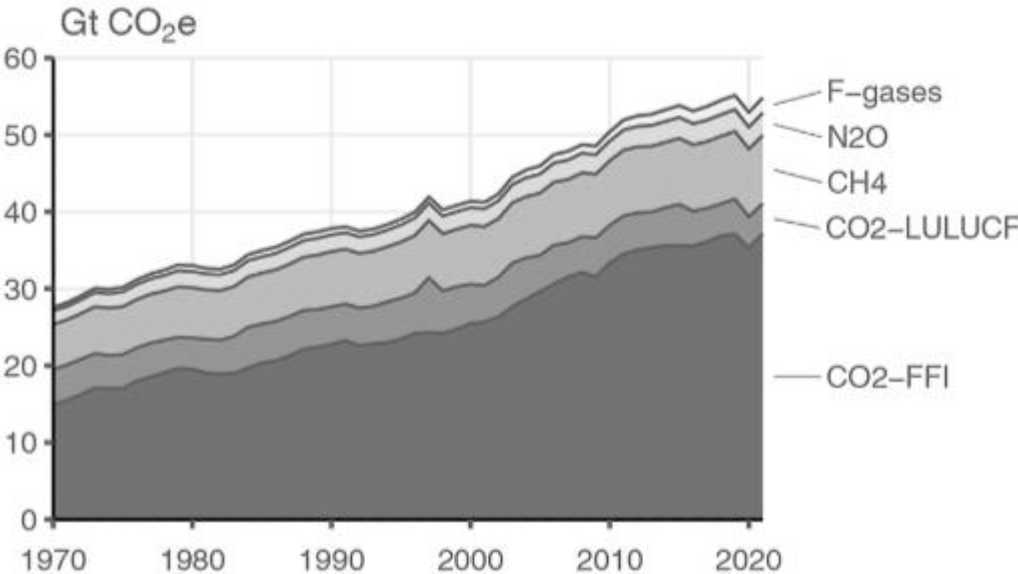

Figure 1 Global Total Greenhouse gas emissions, Land use, land use change (LULUCF) and Fossil Fuel Industry (FFI), [1].

resources has had adverse effects on the planet and most importantly, the quality of human life. The rise in CO_2 levels, which have now reached approximately 420 parts per million (ppm), according to the National Oceanic and Atmospheric Administration, can be seen in Figure 1 [1].

This steady and alarming increase in the CO_2 levels has caused the average global surface temperature of the Earth to rise above 1.2℃ in 2020 [2], Figure 2. This concern goes well beyond a mere

physical phenomenon; it extends to the disruption of agriculture, economies, and quality of human life at the grassroots level.

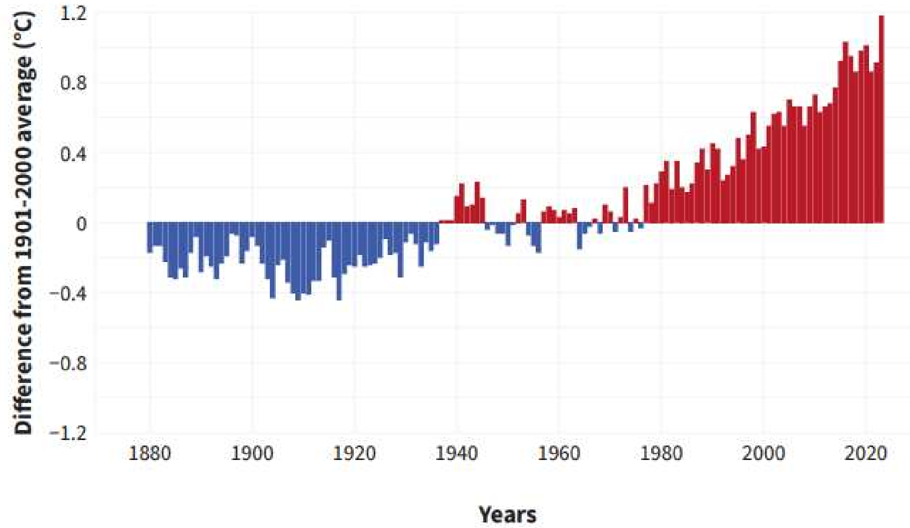

Figure 2 Change in average surface temperature, blue bars= cooler than average, red bars= warmer than average, from [2]

Additionally, because of the rise in average temperature, arctic sea ice has been melting at a rate of ~12.2% per year per decade, with approximately 151 billion metric tons of ice sheet melt occurring annually, and sea levels rising by a total of 104mm since 1990, Figure 3. [3]

	Reference	**Mass change rate (Gt yr^{-1})**					
		2000–2004	**2005–2009**	**2010–2014**	**2015–2018[a]**	**2000–2018[a]**	**2003–2018[a]**
Glaciers	This study	−227 ± 25	−257 ± 22	−284 ± 23	−292 ± 24	−264 ± 16	−272 ± 16
Greenland Ice Sheet	IMBIE[7] minus this study (Greenland Periphery)	−94 ± 65	−206 ± 56	−267 ± 57	−152 ± 64	−181 ± 31	−205 ± 32
	Smith et al.[9]						−200 ± 24
Antarctic Ice Sheet	IMBIE[8] minus this study (Antarctic and Subantarctic)	−36 ± 118	−93 ± 104	−214 ± 94	−157 ± 87	−121 ± 104	−143 ± 104
	Smith et al.[9]						−118 ± 48

Figure 3 Mass change rate of glaciers, from [3].

The damage due to climate change may be permanent. However, renewable energy has emerged as our best answer to mitigate these effects. When we think of renewable energy, the thought needs to be holistic, in the sense that every feasible, available technology must be utilized to fully harness the suns energy received by the earth. In the last decade, we have significantly improved our understanding of non-conventional renewable energy technologies and implementing them all over the world. Below is Figure 4 showing the capacity of all renewable technologies installed until 2023 [4]. Among these technologies such as solar, wind, geothermal, bioenergy, etc., solar is currently our best option. The Solar PV market is one of the fastest growing in the world, with ~13% growth per annum [5]. Most importantly, the cost of electricity generated by solar is currently the lowest [6].

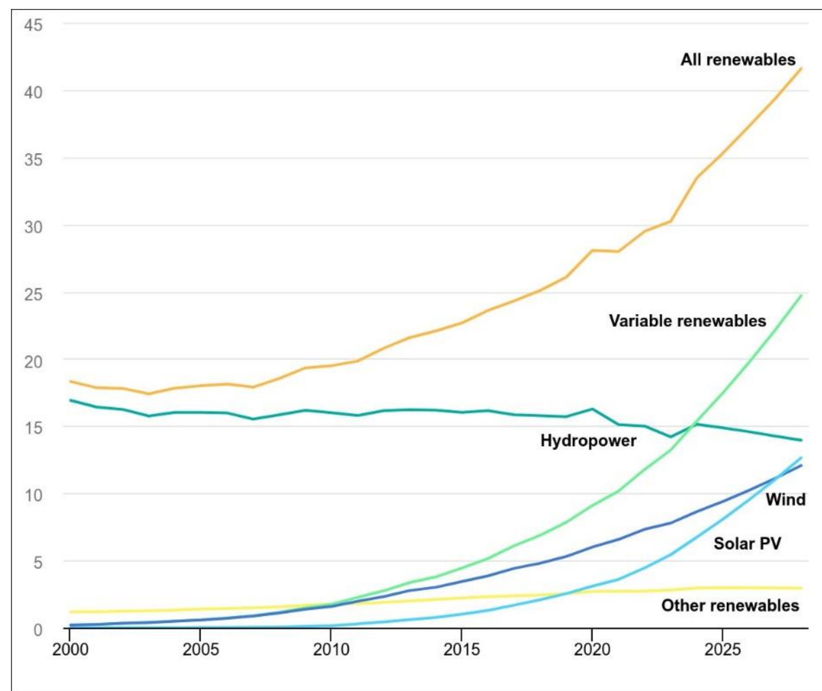

Figure 4 Total installed capacity of all renewable technologies and prediction till 2030, [4]

1.2 Understanding Materials:

Materials are typically divided into semiconductors, metals, and insulators, and further sub-divided into crystalline and amorphous. Crystalline materials are those where the material has a specific arrangement of atoms that is continuously repeated, almost indefinitely. Amorphous materials have a specific arrangement of atoms but there is little to no repeating order. Most metals exhibit crystallinity and polymers such as plastics are amorphous. Further, crystallinity can be sub-categorized into monocrystalline and polycrystalline (px) materials. Monocrystalline materials have the arrangement of atoms that are repeating and are in one single direction in 3-dimensional space. Polycrystalline materials have the arrangement of atoms that are repeating, but in different directions of 3-dimensional space. Each arrangement of atoms in different directions is known as the grain of the bulk material and the

Figure 5 The periodic table of elements, from [7]

space between each adjoining grain is known as the grain boundary. Figure 5 shows the periodic table of elements, with common semiconductors such as Ga, Ge, Te, Sb, Si, etc., metals and alkali metals such as Fe, Al, Co, Ni, Zn, Na, etc. [7]. The primary categorization of metals, semiconductors and insulators originates from their electronic properties and how they emerge. The property that makes this distinction is called the band gap. The band gap can be most easily explained by the properties of electrons in atoms. In an atom, electrons orbit the nucleus at distinct, quantized energy states. Since

these energy states are different from one another, electrons are only allowed to move at a certain energy. This gives rise to bands of energy states. Notably, two bands are formed, the conduction band and the valence band. The conduction band is the region of free electrons that are not bound to an atom and are free to move along the conduction band. The energy levels below the valence band are states of electrons that are bound to their respective atoms and not allowed to move. Between these two bands is the bandgap, a forbidden region where no electrons may be found and have no energy states. Since no energy state can be occupied in the bandgap with an electron, this bandgap is defined as the minimum energy required to separate or free the electrons from their host atoms under the valence band and excite them into the conduction band. Instead of imagining an empty spot from where the electron has left from the valence band, physicists have coined the term “holes”, for when an electron is excited into the conduction band and leaves behind a vacancy. Within the bandgap is a statistical construct, called the Fermi-level, where there is a 50% probability of finding charged carriers. This excitation of the electron from the valence to the conduction band leads to the formation of the electron-hole pair and is fundamental to understanding how semiconductors work. Additionally, these generated charge carriers cannot exist in perpetuity and need to recombine to achieve the lowest energy state as dictated by thermodynamics. This recombination is another key property of semiconductors and requires understanding to explain this work.

In contrast to semiconductors, insulators have a very large bandgap, meaning that a large amount of energy will be required for these materials to generate electron-hole pairs, and therefore, these materials have poor electrical conductivity. Metals, on the other hand, have no defined bandgap, and the valence and conduction band overlap. This allows electrons to move freely in a group, allowing for high conductivity of electrically charged carriers. An illustration of the bandgap can be seen in Figure 6 [8].

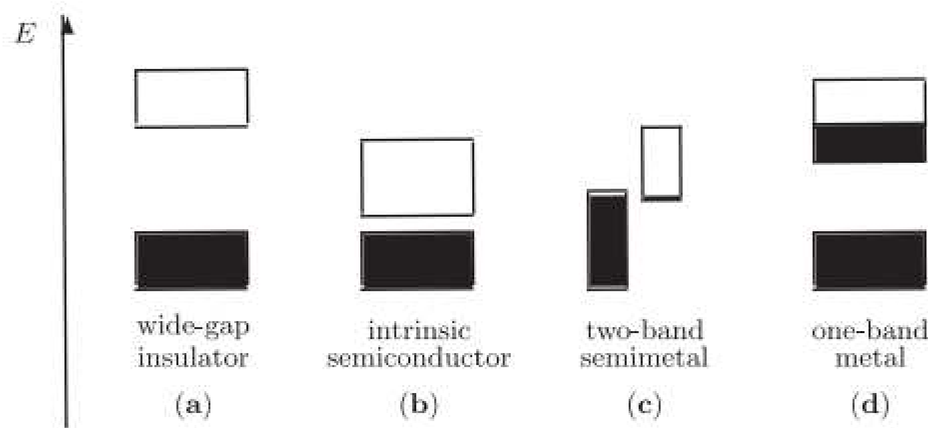

Figure 6 Illustration of the bandgap in materials, from [8].

Interestingly, semiconductors' electronic properties can be modified to improve the electrical conductivity, voltage, and hence, power generated or converted. By using only trace amounts of additives or dopants as they are widely known, the valency of atoms within the semiconductors can be changed. This change in valency denotes a change in the number of free charge carriers within the semiconductor material, thereby altering its electrical conductivity. Additionally, by carefully controlling the type and concentration of dopants, semiconductor devices can be tailored to exhibit specific electronic behaviors, such as enhanced voltage that may improve power generation. This versatility in modifying semiconductor properties has been instrumental in advancing various fields, from electronics and telecommunications to renewable energy technologies like solar cells and power electronics. Doping in semiconductors can occur in two forms: n-type or p-type, determined by the impurity element introduced. When doped with n-type impurities, the semiconductor lattice gains additional electrons,

augmenting its electron conductivity. Conversely, p-type doping involves introducing impurities that create a deficit of electrons compared to the intrinsic semiconductor, thereby enhancing hole conductivity. Figure 7 illustrates the doping process in silicon, where adding phosphorus or boron atoms

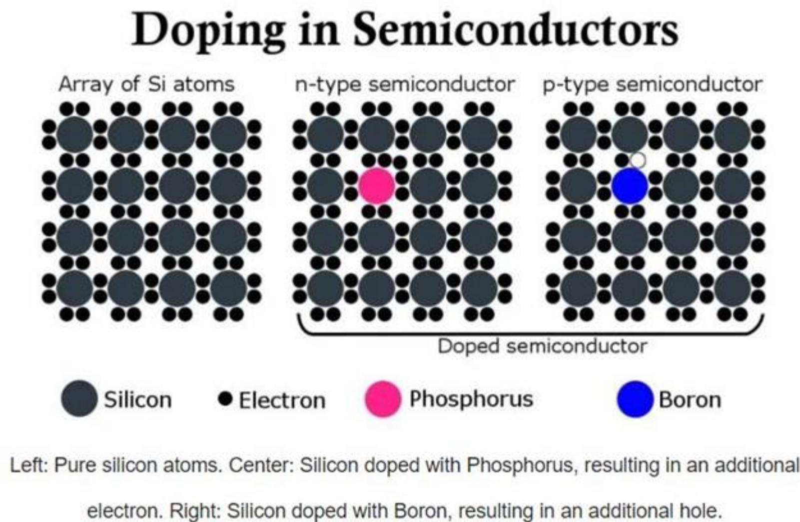

Figure 7 Illustration of doping in a Si semiconductor, from [9].

results in n-type or p-type doping, respectively [9]. Lastly, the charged carriers that have been generated cannot last indefinitely. They tend to return to their lowest energy state as dictated by the second law of thermodynamics. This tendency is known as recombination of the carriers where the electrons from the conduction band fall back into the valence band and recombine with holes. Recombination also occurs at the surface of semiconductors, where the repeating order of the arrangement of atoms abruptly stops and leaves behind open bonds of atoms. These open bonds are sites of high electrical activity. When the charged carriers move toward the surface along the bands, they experience recombination due to this. This recombination can be measured by measuring the lifetime of the charged carriers. Recombination within and on the surface of the material is most often a non-desired effect and researchers have worked on mitigating it.

1.3 What is the P-N junction and how does a solar cell work?

As explained in the previous section, a semiconductor that is doped with a P-type material has a surplus of holes and a semiconductor that is N-type doped has a surplus of electrons. When these two types of semiconductors are joined together, it creates a P-N junction where electrons from the N-doped semiconductor and holes from the P-doped semiconductor are attracted to one another, as explained by Coulombic attraction. This process continues until an equilibrium is reached, leaving behind an area depleted of free electrons and holes (charged carriers), known as the depletion region. Consequently, a gradient in the form of an electric field is established across the depletion region. This electric field acts as a barrier to the further attraction of charge carriers and is termed the built-in potential, which is the maximum amount of voltage that can be extracted. The open circuit voltage (V_{oc}) is the amount of voltage that can be generated and is closely related to the built-in potential. In an ideal case, V_{oc} is equal to that of the built-in potential. The number of the charged carrier in the solar cell also plays an important role. The higher the number of charged carriers, the greater the potential of extracting current.

Photovoltaics are semiconductor materials that convert sunlight into energy in the form of electricity. Sunlight comprises photons of various wavelengths and hence, energy. Each semiconductor material has a defined bandgap energy. Hence, only photons with energy more than or equal to the bandgap of these materials can excite and separate the charged carriers. Conventionally, photovoltaics are made up of a P-N junction, as explained above. When photons from sunlight with enough energy to generate charged carriers strike a PV device, the electrons are promoted to the N-type region and the holes to the P-type region. When an external circuit or load is connected to the solar cell, the built-in

potential helps drive the flow of electrons through the external circuit, thereby generating electrical power. An illustration of the PN junction band diagram can be seen in Figure 8 [10].

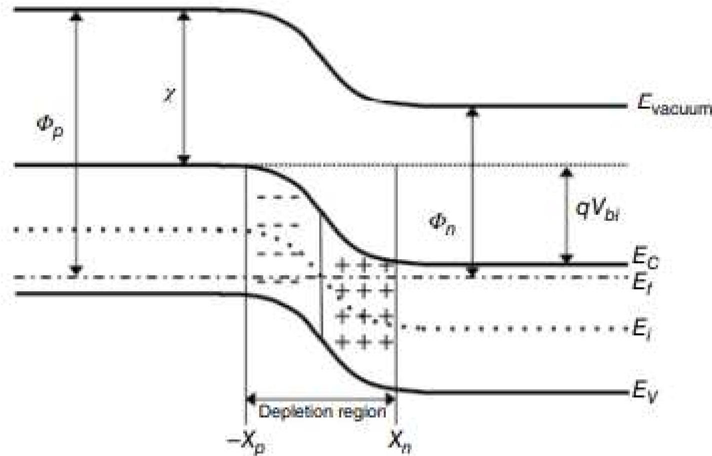

Figure 8 Illustration of bandgap in a PN junction; left: P-doped, right: N-doped, from [10].

1.4 What is CdTe and CdSeTe?

Cadmium Telluride (CdTe) and Cadmium Selenide Telluride (CdSeTe) are semiconductor materials with promising applications in photovoltaics, photodetectors, and optoelectronic devices.

CdTe is a compound semiconductor composed of cadmium and tellurium atoms. It has a direct bandgap, making it suitable for absorbing sunlight efficiently, which is a crucial property for solar cell applications. Additionally, CdTe solar cells are made as thin films, meaning the thickness of the materials used ranges from 100 nm to 3.5 micrometers. CdTe solar cells have gained significant attention due to their high-efficiency potential, low-cost fabrication processes, and compatibility with large-scale production techniques like thin-film deposition. These attributes position CdTe as one of the leading contenders in the solar energy market, offering a cost-effective and scalable solution for renewable energy generation.

CdSeTe, on the other hand, is a ternary compound semiconductor that combines cadmium, selenium, and tellurium atoms. By incorporating selenium into the CdTe lattice, the bandgap of the

material can be adjusted, allowing for further optimization of its optical and electrical properties. This tunability makes CdSeTe a promising candidate for advanced solar cell technologies, where precise control over the bandgap is crucial for achieving higher efficiencies and broader spectral absorption. Additionally, CdSeTe-based materials show potential in other optoelectronic applications, such as photodetectors and light-emitting diodes (LEDs), due to their versatile optical properties and compatibility with semiconductor processing techniques. Both CdTe and CdSeTe hold promise for advancing solar energy technology and expanding the range of optoelectronic devices.

Finally, solar cells, as explained in the previous sections are noiseless, have nearly no moving parts, and are manufacturable at scale. Among all the commercial solar photovoltaic technologies, monocrystalline silicon dominates the market. However, crystalline silicon has significant limitations with high efficiency demanding extremely high semiconductor purity. To combat this stringent nature of c-Si PV technology, CdTe PV has been at the forefront of research for decades. It is a relatively forgiving semiconductor in terms of purity and processing from raw materials to panels. CdTe also benefits from a significantly higher manufacturing throughput in a less energy-intensive manufacturing throughput relative to c-Si PV, and the cost of energy per unit of electricity on a utility scale is significantly lower than c-Si PV [11].

1.5 CdTe research at the Center of Advanced Photovoltaics

Previous sections gave us a preliminary understanding of the photovoltaic effect and how electricity is generated from it. However, at CSU's Center of Advanced Photovoltaics, the PV cell is not just made of one P-N junction on a substrate. Instead, on a glass substrate, there's a transparent tin oxide layer doped with fluorine (FTO) to make it highly conductive, followed by another transparent layer made of magnesium-doped zinc oxide ($Mg_xZn_{1-x}O$, (MZO)), which allows the transmission of a wider spectrum of sunlight, specifically, the lower wavelengths. Then comes the thickest layer, about 3.5 µm,

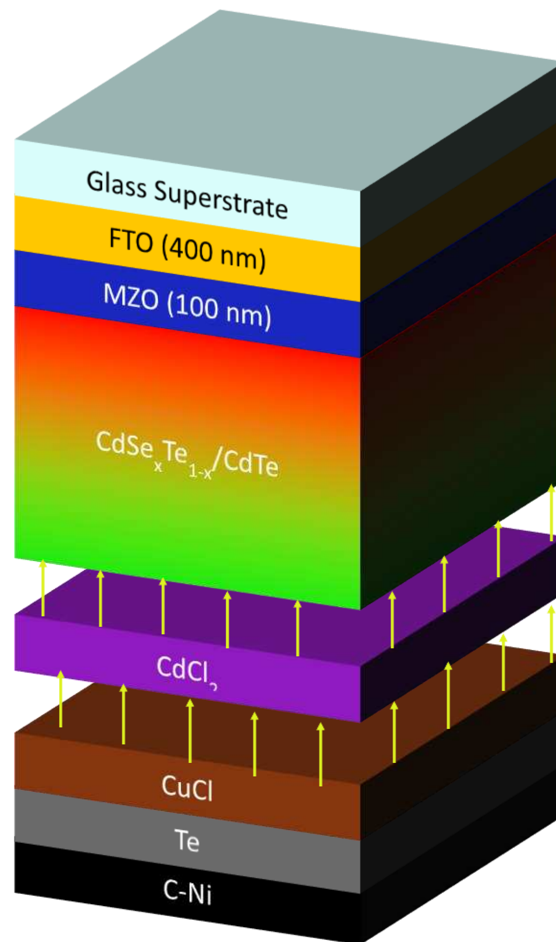

Figure 9 Structure of the baseline CdTe thin film photovoltaic device at CSU.

made of the semiconducting $CdSe_xTe_{1-x}$ (x=0.4) (CST40) and CdTe, wherein Se is diffused to create a gradient and tune the bandgap to about 1.45 eV. This is deposited with a physical vapor deposition (PVD) method, where a source containing the material is heated and the vapor of the material is deposited

onto the glass superstrate that is maintained at a temperature colder than the source. This architecture creates a structure where one side has excess negative charge (n-type) and the other has excess positive charge (p-type), resulting in a P-N junction. After deposition of the CST40 layer, it is treated with cadmium chloride by PVD to passivate the grain boundaries and interfaces therein, to reduce recombination. This is followed by a Cu doping treatment by CuCl to form an ohmic contact, a metal-to-semiconductor transition that reduces the resistance experienced when extracting current. Following this is an additional layer of tellurium 30 nm thick, which is p^+ (highly p-type) in nature. The purpose of adding a layer of Te is to lower the resistance when extracting current. This step is followed up by a paint of C and Ni, to form an electrode for better conductivity. Finally, the large area of the photovoltaic device is divided into 25 small area cells and contacted with Indium on the FTO to measure electrical parameters. This makes a baseline solar cell at Colorado State University. With this architecture shown in Figure 9, a context has been provided to better understand the research and fabrication of the solar cells at CSU.

1.6 Understanding the limit of CdTe solar cell performance.

Solar cell technology has made significant advances since as early as the 1920s. However, the thermodynamic maximum limit of power conversion efficiency of a solar cell as a function of the bandgap of the material was calculated in 1961 by William Shockley and Hans Queisser. It explains in detail that the maximum power conversion efficiency of a solar cell is achieved when all photons from sun radiation with energy greater than the bandgap are absorbed and the excess energy is minimized. Hence, for a single-junction solar cell, the maximum thermodynamic Shockley Queisser (SQ) limit can be calculated if the bandgap of the material is known. This concept is a cornerstone in understanding what limits the performance of the solar cell and how it can be improved [12].

Current CdTe single junction solar cells have vastly improved since their conception in the 1950s, but leave room for significant improvement. For a bandgap of CdTe with a Se concentration of 33%, the bandgap is roughly 1.45 eV. For this bandgap, the SQ limit is calculated to be ~32.3%, with an open circuit voltage (V_{oc}) of ~1.1 V and a short circuit current density (J_{sc}) of 32.0 mA/cm^2. However, the current record px-CdTe solar cell is at 21±0.4 % efficiency, 30.25 mA/cm^2 J_{sc}, and 0.875 V. It is clear from the established record efficiency px-CdTe solar cell, that the limiting parameter is the open circuit voltage. Even though doping is done to improve it, the current record is only 75.8% of the maximum voltage possible. This is the primary motivation for this research and three hypotheses were formed relevant to this. Each hypothesis has been given its own chapter, with a background established in the first section, at the end of which the hypothesis statement is stated in italic. The proven/disproven status of each hypothesis is stated in italic too, and the discussion chapter aims to provide more insight into the thought process for this research.

Chapter 2: LITERATURE REVIEW

A review of published literature was conducted to understand the experimental and theoretical aspects that can lay a foundation for the research performed here. As noted in the previous chapter, the open circuit voltage is the most underperforming parameter. Hence, this literature review is largely focused on limiting factors and methods of improving voltage in CdTe thin film photovoltaics.

To understand the extent of this review, the conventional and most recent methods of fabrication of CdTe PV must be explained. In many ways, these methods of fabrication and device architecture are similar to those at CSU. In a comprehensive review paper by Scarpulla et al, the methods of CdTe PV fabrication are elaborated. The first step is the deposition of an n-type transparent conducting oxide (TCO) on a low iron content glass, followed by deposition of a Se-graded CdTe thin film using vapor deposition. This is followed by a $CdCl_2$ treatment that promotes grain growth and passivates the grain boundaries. A Cu doping treatment is performed after the $CdCl_2$ process to form an Ohmic contact and dope the absorber n-type to boost voltage. And further appropriate metal contacts and electrodes to improve conductivity, resulting in a completed solar cell. Finally, the most notable point the authors made was that improving the V_{oc} and reducing the recombination of carriers within the bulk of the material and at the surface are key steps to get closer to the SQ limit [13].

Historically, CdTe thin films have been doped with Cu to improve the voltage and current extraction, but Cu doping has shortcomings of its own. The review on the limitations of Cu paints a picture of why doping is required, but moving away from Cu doping and on to better alternatives is currently being explored.

2.2 Limitations of Copper Doping

Despite Cu doping's widespread use, copper comes with several drawbacks that limit the performance of Cu-doped devices. Undoped CdTe typically exhibits an intrinsic hole density of approximately 1–5 x 10^{14} holes/cm^3, primarily due to the thermodynamic tendency of cadmium vacancies to form at high temperatures [14]. Unfortunately, incorporating copper as a dopant has only a minimal effect on the bulk hole density of CdTe. Even with copper doping, bulk acceptor concentrations rarely surpass 10^{15}/cm^3 when measured by CV, often failing to achieve even a single order of magnitude increase. Yang et al noted that increasing the concentration of Cu does not mean a corresponding increase in hole concentration, and Kucys et al proposed some primary mechanisms that have been identified to collectively elucidate the poor doping performance of copper: self-compensation, low activation, and grain-boundary segregation [15], [16].

Copper tends to distribute unevenly throughout the polycrystalline bulk of CdTe [17]. First principles studies have revealed that it is energetically favorable for copper to migrate and settle at the

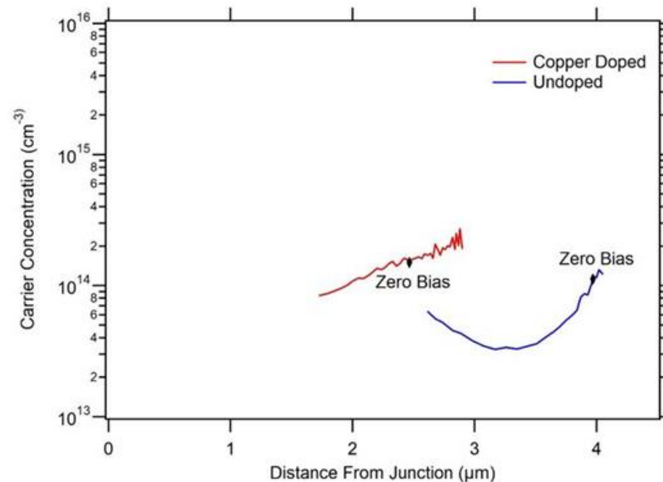

Figure 10 Carrier concentration vs depletion width of Cu doped and undoped CdTe cells, from [14].

grain boundaries, a discovery supported by TEM investigations [18], [19]. This phenomenon partly explains why the carrier concentrations in Cu-doped CdTe are typically several orders of magnitude lower than the copper incorporation. However, the mobility of copper within CdTe poses additional challenges.

Interstitial copper exhibits rapid diffusion in CdTe, even at room temperatures, potentially causing various issues. This is exacerbated during the $CdCl_2$ passivation treatment, wherein the temperature and operating conditions promote the diffusion of Cu to the front of the absorber and hence, its mobility during normal operating conditions can lead to long-term stability problems in CdTe devices [20]. Photovoltaic performance may experience significant fluctuations as copper accumulates at grain boundaries and interfaces.

Additionally, Jones et al performed fitting of data of Cu concentration within a CdTe film and observed that Cu has a slow and fast diffusing component, attributing the fast component to grain boundary diffusion and the slow one to intra-grain diffusion. The diffusivities of Cu in a sample that has been treated with $CdCl_2$ were measured to be $5*10^{-8}$ cm^2/s along the grain boundaries and $8*10^{-10}$ cm^2/s within the grains. This further validates the migration of Cu to the front of the absorber [21].

Shimpi et al., fabricated a device using $CdSe_xTe_{1-x}$ and CdTe to tune the bandgap with Se grading, optimized the thickness of each layer through several iterations, and varied the $CdCl_2$ treatment, with a standard Cu doping procedure and measured the efficiency of a small area cell (0.65 cm^2) to be 19.49%, with a V_{oc} of 870 mV. Another sample with an anti-reflective coating that prohibits the reflection of sunlight when it strikes the glass showed an efficiency of 20.14%, with a V_{oc} of 875 mV. This research was performed at CSU and still is the best-performing research institute cell. However, the V_{oc} remains at under 75% of the SQ limit [22].

Hence, we establish that Cu has several drawbacks and that an alternative doping approach may be required to achieve higher V_{oc}. This has been accomplished by P-type doping of CdTe thin film PV devices by Arizona State University and the National Renewable Energy Laboratory (NREL).

2.3 P-type doping in monocrystalline/MBE grown CdTe PV devices

Zhao et al at Arizona State University demonstrated a monocrystalline CdTe device grown with molecular beam epitaxy (MBE) with >1V V_{oc} by using a MgCdTe barrier layer to electrons and an

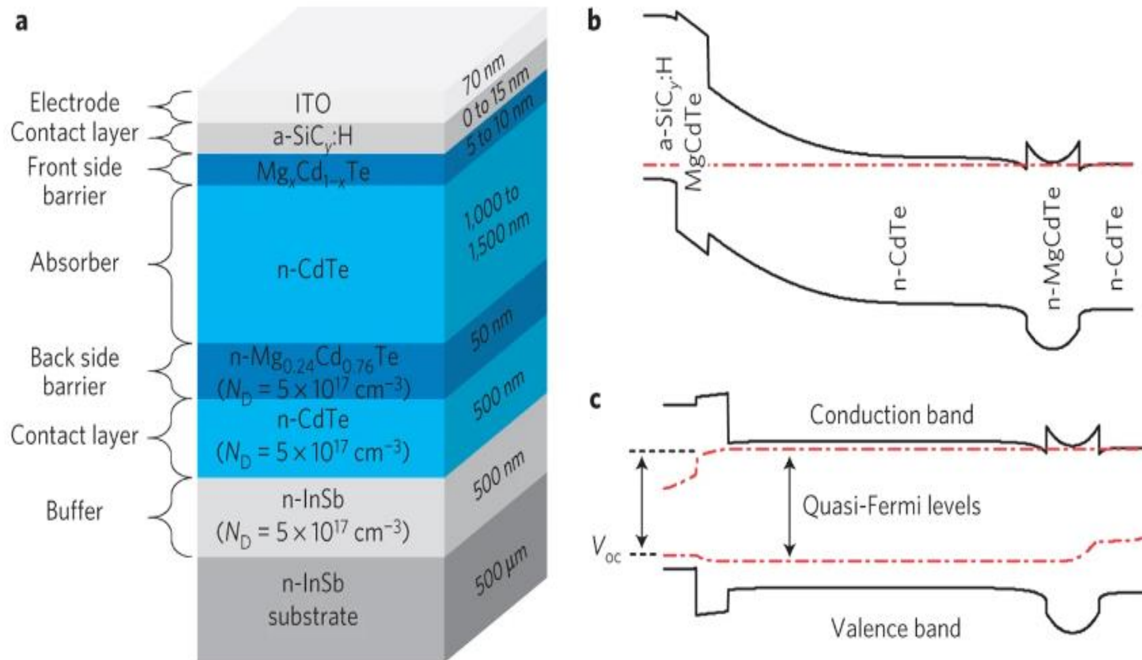

Figure 11 Device structure and band diagram of ASU's 1V Voc CdTe device, from [23].

amorphous silicon heavily p-type doped hole selective layer. The device fabricated demonstrated a 17% power conversion efficiency. This improvement in voltage brings CdTe thin films closer to the SQ limit of ~1.2 V, as a function of the specific bandgap. The device structure and band alignment in an open circuit and at equilibrium can be observed in Figure 11, respectively [23].

Employing phosphorus for doping single crystal CdTe, Burst et al., achieved a hole density of 10^{17} cm^{-3}, 50% dopant activation (Figure 12), and minority-carrier lifetimes of several hundred nanoseconds [24]. As a result, an open circuit voltage of >1 V was observed in several samples. At the time, this was a highly influential finding, indicating that CdTe thin films can certainly reach 1V V_{oc}, close to the SQ limit.

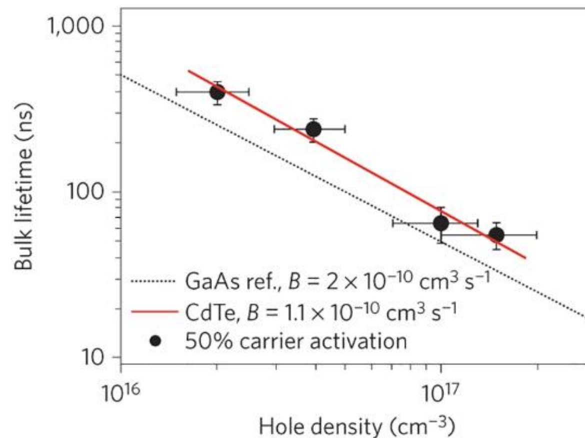

Figure 12 carrier lifetime in the bulk of MBE grown CdTe vs hole density, with P doping, [24].

Farrell et al., using molecular beam epitaxy (MBE), demonstrated arsenic incorporation as high as 7 x 10^17 atoms/cm^3, with acceptor concentrations exceeding 5 x 10^16 holes/cm^3 achievable. Moreover, this study provided clear evidence that arsenic incorporation in CdTe significantly improves when conducted in the presence of a cadmium overpressure of approximately 20%. An arsenic cracker operating at 1000°C was implemented to dissociate native As_4 molecules, which are not dopants in CdTe, into As_2. Despite these efforts, the as-grown films exhibited very low carrier concentration until a subsequent activation anneal was performed, resulting in a reported 50% activation rate [25].

Even though these studies show V_{oc} of 1V, and high carrier concentrations, it is important to note that the devices in these investigations were monocrystalline CdTe. Current polycrystalline CdTe PV devices come close to the 1V mark but do not exceed it and efforts to do so have failed. The current theory is that the grain boundaries in px-CdTe have a deleterious effect on the voltage and hence may be difficult to reach the true SQ limit.

2.4 Group V doping in polycrystalline CdTe PV devices

McCandless et al. successfully incorporated phosphorus, arsenic, and antimony into px-CdTe thin films using vapor transport deposition techniques, albeit with varying degrees of success in activating the respective dopants [26]. Figure 13 illustrates the incorporation and activation rates observed in this

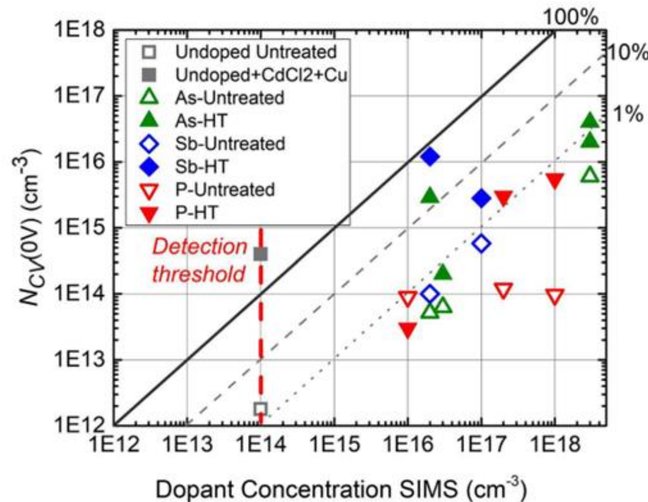

Figure 13 Carrier concentration vs Dopant concentration in px-CdTe samples, [26].

study. From this investigation, it is noted that carrier concentration for As-doped CdTe is highest among all group V dopants.

Similarly, Danielson et al. utilizing co-sublimation of a CdTe ingot doped with As (CdTe:As) and a pure Cd source achieved Voc greater than that of Cu in Se graded CdSexTe1-x/CdTe devices. Figure 14 shows the performance gains of an As doped device compared to a Cu doped device [27].

Dopant	Jsc (mA/cm^2)	Voc (mV)	FF (%)	η (%)
Undoped	25.8	759	33.1	6.48
Copper	26.5	788	67.5	14.10
Arsenic	26.8	818	76.5	16.79

Figure 14 Electrical characteristics of px-CdTe devices with various dopants, [27].

First Solar reported a 22.3% efficient small area (<= 0.5 cm^2) cell in 2023. The other cells on the same glass plate had some of the highest voltages recorded for small-area cells, with the highest being 917 mV, measured at First Solar itself. The authors attributed the voltage improvement to doping the absorber with As during film deposition and the fill factor improvement using an anti-reflective coating to boost absorptance on the glass side of this sample and increased the lifetime of carriers compared to previous studies. The cell exhibited some important characteristics wherein the lifetime of carriers as measured through the glass was approximately ~400 ns and a carrier concentration of 10^{16} cm^{-3}. In conclusion to this study by Mallick et al, the authors note that improving recombination and activation of arsenic (the ratio of incorporated dopant atoms to ionized acceptors) indicates a pathway toward 25% efficient solar cells [28].

Lustig et al. investigated Arsenic doping by employing Cd_3As_2 as the doping source material. This study involved heat treatment of the material and incorporating As in CdSeTe only and CdSeTe/CdTe bilayer device architectures. Energy efficiencies of upto ~12% have been reported in the CdSeTe only films and, up to 19% in the CdSeTe/CdTe bilayer films [29]. This method at the time was novel, and was aimed at exploring a different pathway of As doping compared to the traditional one, where an ingot of CdTe was doped with As (CdTe:As).

Metzger et al investigated a similar approach using Cd_3As_2 as the dopant source charge and achieved a V_{oc} of 856 mV, power conversion efficiency of 20.8% in a px-CdTe thin film solar cell. The authors also reported a high carrier concentration of ~10^{16} cc^{-1}, and finally noted that the diffusion of As in the film is slower than that of Cu [30].

The voltage gain and performance improvements with As doping are not as close to what was envisioned. However, among the rest of the group V dopants and compared to Cu doping, it does offer a promising avenue and this study explores it by implementing Cd_3As_2 as the doping source charge.

2.5 Oxide Deposition/Formation and passivation

It has been long-standing knowledge that interface and surface passivation of semiconductors is crucial to obtaining low surface recombination rates and high carrier lifetimes. In this work, passivation and the literature review refer to the 'back' surface of CdTe films, and hence, the interface/surface of the hole contact. Since most semiconductors suffer from un-passivated surfaces, the carriers tend to recombine and cause a loss of current. Additionally, the un-passivated nature can cause abnormal band bending and may inhibit the voltage. There has been a significant amount of work done all over the world to ensure the above-mentioned detrimental effects are mitigated. There has been a unanimous agreement that oxides on the surface of CdTe thin film photovoltaics are passivating. The extent of this passivation can be characterized by Time-Resolved Photoluminescence, wherein the decay kinetics of emitted photons due to recombination are analyzed over time and the chemical/physical properties of the oxide itself can be characterized by X-ray photoelectron spectroscopy, surface potential measurements by Kelvin Probe Force Microscopy (KPFM) Electron Beam-Induced Current (EBIC), etc. With this preliminary knowledge in mind, we will now look at some of the work in the formation and characterization of passivating oxides that has been done.

At Colorado State University, Tellurium has been traditionally used as part of the back contact, by depositing with Closed Space Sublimation. Experimental findings over a significant period of time have indicated that a 30nm Te deposition improves voltage and fill factor [31].

A study by Kephart et. al demonstrated Al_2O_3 as the best candidate for passivation of the CdTe back surface. This Al_2O_3 was sputter deposited and the effects of varying thicknesses of the same were investigated on hetero and double heterostructures (Al_2O_3/CdSeTe, Al_2O_3/CdSeTe/Al_2O_3). The authors note that the highest passivation known to them occurred at the back surface because of the double heterostructure. This heterostructure had a thicker absorber of CdSeTe (2.5 micron) as compared to previous samples (0.6 micron – 1.3 micron) and the thickness of Al_2O_3 was 20nm. Increasing the thickness of the absorber dramatically improves the lifetime of the carriers from 36 ns to 430 ns, (Figure 15) [32].

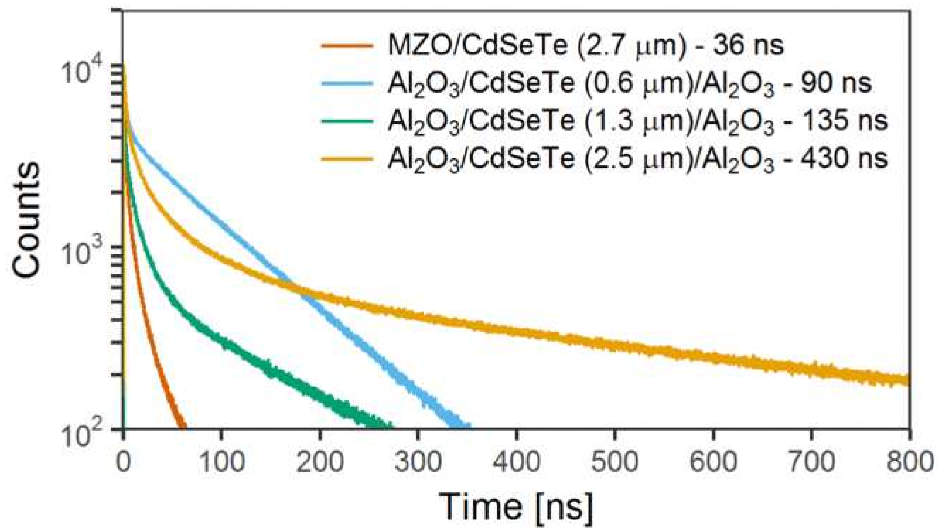

Figure 15 TRPL emission spectra of Heterostructures with Al2O3, [39].

This was further corroborated by Danielson et. al., by sputter depositing a film of Al_2O_3 and characterizing the lifetime of carriers with TRPL. Most importantly, this presented somewhat of a "paradigm shift" as the authors called it, since this deposition was on a $CdSe_xTe_{1-x}$ surface without a layer of CdTe. As a result, lifetimes as high as 10 microseconds. They noted that, most of the passivation is being carried out at the back surface, following the sputter deposition of the aluminum oxide. Measurement of the back surface recombination velocity was performed as well, and the surface recombination velocity was found to be an order of magnitude lower than the standard baseline samples that had a Te film as part of the back contact [33].

Additionally, Perkins et. al have proposed an alternative mechanism where well passivated interfaces of CdTe and Al_2O_3 indicated an increase in the Te^{4+} photoelectron signal during XPS measurements. The conclusion drawn from this result noted that a tellurium oxide layer may be forming under the Al_2O_3 during the $CdCl_2$ treatment process and that is providing chemical passivation at the surface [34].

At the University of Illinois Chicago, High angle annular dark field (HAADF) TEM imaging was performed to characterize TeO_2 on a CdTe film formed by exposing the sample to ambient air. Additionally, J. Farrell et al characterized a n-TeO_2 formation on polycrystalline CdTe by Electron Energy Loss Spectroscopy (EELS). This study was performed solely to characterize this metal oxide and the mechanism of formation of this oxide was yet unknown. Figures 16 and 17 show the HAADF and EELS

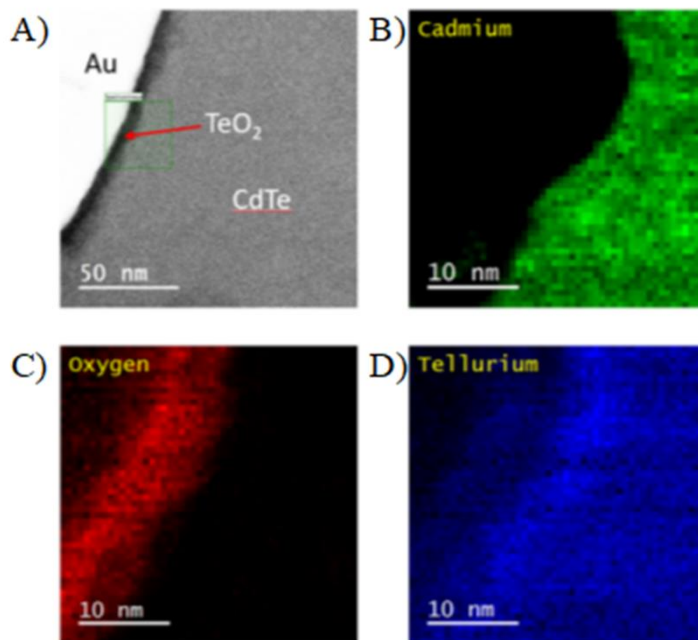

Figure 16 HAADF STEM image of TeO2 on a CdTe surface.

analysis. The HAADF in this investigation revealed the darker area annotated with the red arrow due to the significant presence of oxygen around the surrounding CdTe region. The EELS analysis reveals the

two distinct peaks of Te-M orbital edge and O-K orbital edge, which very distinctly signify the presence of TeO_2. [35]

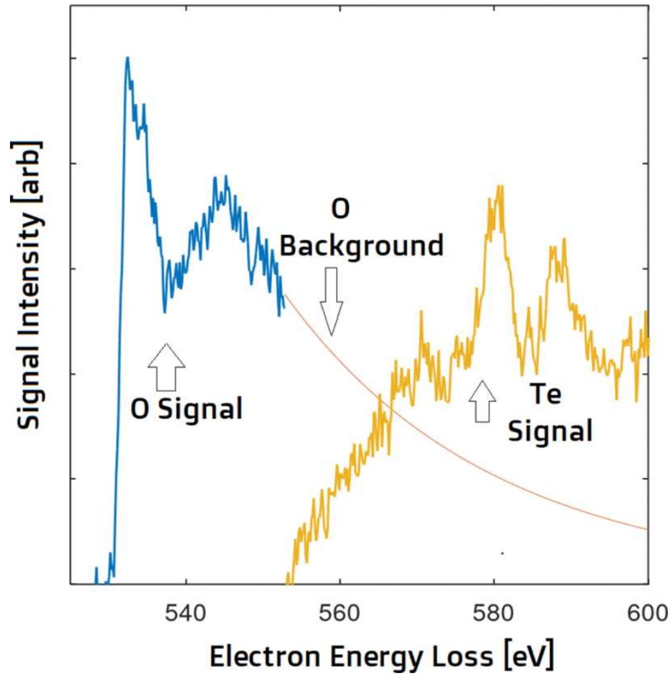

Figure 17 EELS spectra of Te and O showing a double peak and confirming presence of TeO2, [35].

A high-resolution cross section TEM study by Fernando A. Ponce revealed that the interface between CdTe and TeO_2 is perfectly coherent for the crystallographic orientation studied and has a one-to-one relationship between the crystal planes of the oxide and CdTe. More importantly, their analysis of the chemical nature shows that Cd at the interface is unstable and can be easily displaced by oxygen and leaves the Te sublattice only slightly modified [36].

Finally, in a study by Yi et al, on the surface oxidation of polycrystalline CdTe solar cells grown on tungsten-coated graphite and exposed to ambient air for 6 months, the carrier concentration was reported to be $3*10^{16}$ cc^{-1}, an improvement to the V_{oc} from 450 mV to 600 mV and an improvement to the Fill Factor of about 33 % [37].

From the literature survey conducted in this chapter, we note that As doping may provide a promising pathway to directly improving the V_{oc}, metal oxide formation is important to passivate the

surface of CdTe thin films and indirectly improve the voltage. However, the known methods to do so involve the deposition of a metal oxide through instrumental means or an unknown method of forming a native TeO_x at the back surface of CdTe. An investigation of improving upon these methods is investigated in chapters 5 and 6 and the following chapter 3 will explore the equipment, knowledge and expertise that is required for this investigation.

Chapter 3: FABRICATION AND CHARACTERIZATION METHODS

3.1 Introduction

This work focuses on solar cell fabrication and physical and electrical characterization of these cells to help understand the physical phenomenon occurring within the materials used. For the reader to understand the following chapters, this section will introduce the fabrication and characterization techniques used at CSU.

3.2 Superstrate glass information

At CSU's solar Center for Advanced Photovoltaics lab, the first step to making high-efficiency solar cells is to clean the glass upon which the thin films of semiconductors, optical, and conductive materials will be deposited. Pilkington manufactures and supplies the low iron content TEC10, TEC12, and TEC15 glass with a layer of Fluorine doped tin oxide (SnO_2:F) that has a thickness of 400 nm. The nomenclature for the glass comes from the respective resistance, as TEC10: 10 Ω/cm^2 and so on. The washing of the glass involves cleaning it in ultrasonic chambers in a Micro-90 detergent bath to remove contaminants, followed by a slow drying process that prevents streaking of any residual detergent. This process aids in achieving the highest transmission of light through the glass.

3.3 Window layer deposition

Following the cleaning step, the next task is to deposit a 100 nm layer of high-resistance transparent oxide, Magnesium-doped Zinc Oxide (MgxZn1-xO or MZO), using the Radiofrequency (RF) sputtering process. Previously, a window layer of CdS was used in CdTe thin-film photovoltaic (PV) devices. However, MZO material has been proven to improve the current and fill factor [38].

Sputtering involves the expulsion of atoms from a material target due to the impact of high-energy particles. In RF sputtering, an alternating high-frequency (RF) voltage is applied between the

target (cathode) and the anode. The alternating electric field ionizes the process gas, typically argon, creating plasma which is made up of electrons and positively charged ions. These ions are attracted to the target during the negative half-cycle of the RF signal, where they strike the target material, dislodging atoms from it. These dislodged atoms are then deposited onto a substrate positioned above the target.

This sputtering process is carried out at 5 mTorr with a gas mixture of 97% Ar and 3% O2, at a supplied power of 140 W, and with a superstrate-to-target distance of 15 cm. This window layer aids in the transmission of short wavelengths of solar radiation [39].

Figure 18 Picture of the RF sputtering system for MZO deposition.

3.4 CdSexTe1-x and CdTe deposition

Now, the deposition of $CdSe_xTe_{1-x}$ (x=0.4) and CdTe thin films are carried out in CSU's proprietary Advanced Research Deposition System (ARDS) using physical vapor deposition (PVD) in a closed space sublimation (CSS) and superstrate configuration. The ARDS contains 9 stations each containing different materials for the fabrication of solar cells. Each station contains two sources/heaters, the bottom one that heats the material and facilitates vapor flux, and the top one kept cooler than the bottom that heats the substrate to ensure deposition via vapor condensation. The first step was to preheat the glass superstrate to 620℃, followed by the deposition of the semiconductors. This deposition was carried out at 40 mTorr of pressure under ultra-high pure Nitrogen. $CdSe_xTe_{1-x}$ deposition was carried out at 575℃

Figure 19 Top: Picture of the ARDS; Bottom: Picture of the CSS sources inside the ARDS.

bottom source temperature and 420℃ top source temperature, followed by the CdTe deposition, which was 555℃ bottom source temperature and 500℃ top source temperature. The deposition of both films results in a CdTe film with a graded Se concentration throughout the thickness of the film. This structure will be referred to as the 'bilayer' in this work. The $CdCl_2$ grain and grain boundary passivation treatment also took place in the ARDS under the same conditions, with or without breaking vacuum at 387℃ bottom source temperature and 420℃ top source temperature. The $CdCl_2$ treatment leaves an unwanted residue and was rinsed with deionized water before continuing with further fabrication steps. A detailed explanation of the fabrication process is given by D. E. Swanson [40].

3.5 Doping processes

For the baseline or control devices considered in this work, Cu doping is the next step. The Cu doping is carried out in a separate CSS system under 70 mTorr of N_2. The system has 3 stations: Preheat, CuCl dose, and annealing. The temperatures of each of these stations during the doping process,

Figure 20 A picture of the CSS vacuum system for CuCl treatment.

sequentially, are 330°C for both heaters, 170°C and 190°C for the top heater and bottom heater respectively, and 200°C for both heaters.

For the As doped samples, the doping process is carried out in a horizontal bell jar (HBJ) in a similar superstrate and CSS configuration as the ARDS. However, the entirety of this work where samples

are doped with As, the doping is carried out by annealing the deposited films over a source of Cd_3As_2.

Hence, for the As doping process via Cd_3As_2, the top heater in the HBJ is kept hotter than the bottom heater, to ensure no deposition of the source material. The temperature of the superstrate source heater was maintained at 500℃ and the bottom source containing the Cd_3As_2 material at 355℃, for all As doped samples in this study.

Following the doping of either Cu, As or both, a 30 nm layer of Tellurium is deposited as part of the back contact, which facilitates the extraction of holes. This deposition is carried out by evaporation under room temperatures and at 10^{-4} Torr with no active process gas. The thickness of the Te film is determined by a quartz crystal monitor. As the final part of the back contact, a C-Ni paint is sprayed onto the back surface of the film, that acts as an electrode. Finally, to provide better electron contact to measure the parameters, the film is divided into 25 small area cells by delineating with silica beads under a mask and contacting the MZO layer with Indium to improve electron conductivity.

3.6 Electrical characterization:

3.6.1 J-V

The short circuit current density, open circuit voltage and the related fill factor (FF) are the three metrics that determine the power conversion efficiency of the solar cell. The measurements are performed under the illumination of a Xenon arc lamp which simulates the radiation of the sun that travels through 1.5 times the thickness of the Earth's atmosphere, referred to as AM1.5, where the irradiance is 1000 W/m^2. Voltage is applied to the solar cell under this illumination and is swept from -0.8 V to 1.2 V in increments of 25 mV. At each increment, the current is recorded and divided by the cell area, which is measured by a contrast camera with a LABVIEW VI, to finally output the current density, J in mA/cm^2. At zero voltage, the cell is short-circuited, and this is known as the J_{sc}, the short circuit current density. And, at zero current, the circuit of the cell is open and the open circuit voltage, V_{oc}, is

measured. The FF is then calculated by these two parameters and it is the quotient of the ratio of the

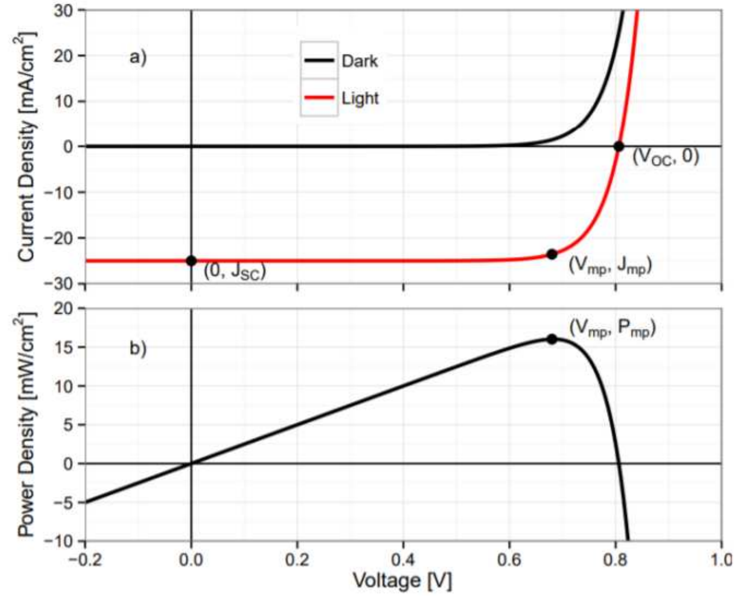

Figure 21 Top: Illustration of a J-V curve under light and dark bias; Bottom: Power density curve acquired from the J-V curve. From [38].

maximum power point (J_{MP}xV_{MP}) and (J_{sc}xV_{oc}). Equations (1), (2), and (3) are used to calculate these parameters, where I is the cell output current, I_L is the light-generated current, I_0 is the leakage current under dark conditions, V is the voltage across the cell terminals, T is the temperature, q is the elementary charge, n is the ideality factor of the diode (a measure of how closely the diode follows the ideal diode equation (Equation (1)) and k is the Boltzmann constant. The efficiency is then output as the quotient of the maximum power and the incident power on the cell [10].

$$I = I_L - I_0[e^{\left(\frac{qV}{nkT}\right)}] \quad (1)$$

$$FF = \left(\frac{V_{MP}I_{MP}}{V_{OC}I_{SC}}\right) \quad (2)$$

$$\eta = \frac{V_{OC}I_{SC}FF}{P_{in}} \quad (3)$$

Figure 21 illustrates the J-V curve and associated parameters in light and dark applied bias conditions.

Further, the shunt and series resistances are important to consider where any losses are coming from. Series resistance is caused by contact resistance between the metal ohmic contact and the CdTe film; it is part of the J-V curve that crosses the horizontal voltage axis. Shunt resistance is caused by a fabrication defect, rather than poor solar cell design. A low shunt resistance causes the carriers to take an alternative pathway, hence reducing current and performance, whereas a high shunt resistance typically means a better current output. It is part of the J-V curve that crosses the vertical current/current density axis. A larger slope for both these resistances means a loss in FF and device performance. An illustrative animation for this can be found on pveducation.org. The J-V measurement setup is shown in Figure 22.

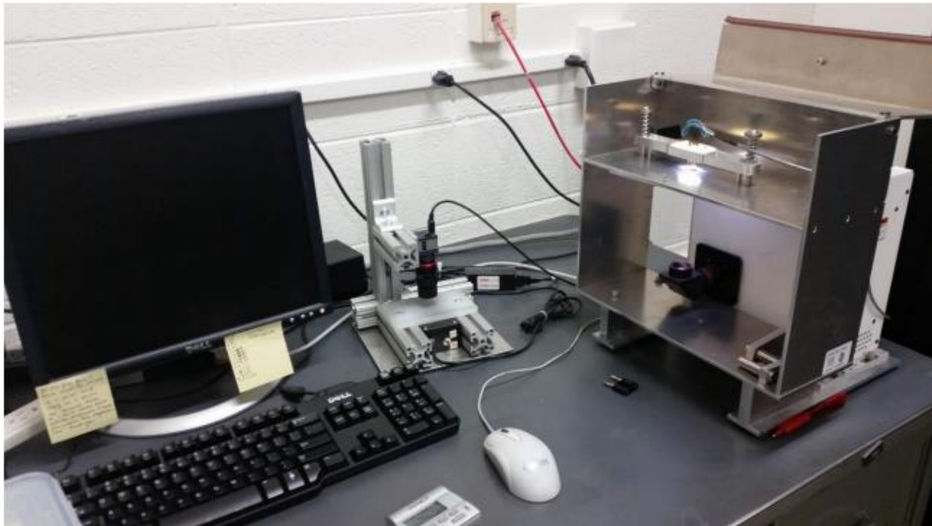

Figure 22 Picture of the J-V measurement setup.

<u>3.6.2 C-V</u>

Capacitance-Voltage measurement is performed by an impedance analyzer that sweeps the applied voltage from negative to positive and measures the change in capacitance as the depletion width changes. So, when a p-n junction is formed as in the case of CST40 and CdTe, the diffusion of electrons and holes creates a depletion region wherein free carriers do not virtually exist. This is analogous to a parallel plate capacitor. This above change in capacitance as a function of the applied voltage can be used to calculate the carrier concentrations and at CSU, the out is given by net hole concentration. The

carrier concentration is traditionally reported at the bottom of the U-shaped belly curve or at the zero-bias point. The net hole concentration is useful to determine the efficiency of the doping, where the activation of the dopant is crucial, and calculated by the concentration of the dopant at the depth in the film to the net carrier concentration at the same depth.

3.6.3 Steady State Photoluminescence:

Photoluminescence helps in measuring the radiative recombination of solar cells. The cell is illuminated under a 638 nm wavelength laser that excites and separates the electrons and holes, generating charge carriers. These charge carriers cannot exist indefinitely and a proportion of them must come to equilibrium by recombining with their counterparts. This recombination emits radiation in the form of light, as the mechanism to the conservation of energy. These photons emitted from the sample are detected by a spectrometer through a fiber optic cable to ensure effective collection of this light and the spectrum is recorded. The interpretation of PL data can be viewed as: if the proportion of radiative recombination increases, the magnitude or intensity of PL increases along with it. This effect is most desired, as the other mechanisms of recombination usually mean defect states exist in the bands, which lower the lifetime of the carriers. For this work, PL data has been measured in an arbitrary unit of Counts per second (CPS) and calibrated data in the units of Photons/m^2.eV.s. This calibration is performed under a halogen tungsten lamp, and the actual irradiance is calculated from the measured and true irradiance values.

3.7 Physical Characterization

3.7.1 Secondary Ion Mass Spectroscopy (SIMS):

SIMS is a powerful characterization tool to map out the elemental composition of a given sample. In this work, we have used SIMS to identify the concentration of Cu and As per cubic centimeter. It operates on the principle of bombarding a sample surface with a primary ion beam, typically

composed of noble gas ions such as Argon or Oxygen and generated by duoplasmatrons or electron ionization and induces the ejection of secondary ions from the sample's surface. These secondary ions are then extracted and analyzed in a mass spectrometer to determine their mass-to-charge ratio (m/z), providing valuable information about the elemental composition and spatial distribution within the sample. SIMS instruments consist of several key components, including an ion source for generating the primary ion beam, a sample stage for positioning the sample, and a mass spectrometer for ion detection and analysis. Additionally, SIMS instruments often incorporate specialized features such as ion optics for focusing and steering the primary ion beam, as well as a detector system capable of high-resolution imaging. In this work, we employ SIMS to measure the concentration of As and Cu through the depth of the film, to determine the diffusion rate of the respective atomic species and to calculate the activation of dopants. This is known as depth profiling, and it is a technique used to analyze the elemental composition of materials as a function of depth beneath the surface. Operating on the principle of sputtering, SIMS bombards the sample surface with a primary ion beam, causing the ejection of secondary ions from various depths within the material. As the primary ion beam continues to sputter material from the surface, the composition of the emitted secondary ions changes, providing information about the elemental distribution with depth. SIMS instruments for depth profiling typically incorporate additional components such as a sputtering ion gun or a focused ion beam (FIB) to remove material layer by layer, allowing for precise depth control. Data analysis in depth profiling SIMS involves correlating the detected secondary ions with the depth at which they were generated, often through calibration with standards or known depth profiles. By measuring the intensity of specific ions as a function of depth, concentration profiles of elements within the material can be obtained, offering valuable insights into material composition, layer thicknesses, and interfaces. All SIMS measurements in this work were carried out at Eurofins EAG laboratories.

3.7.2 X-ray Photoelectron Spectroscopy (XPS)

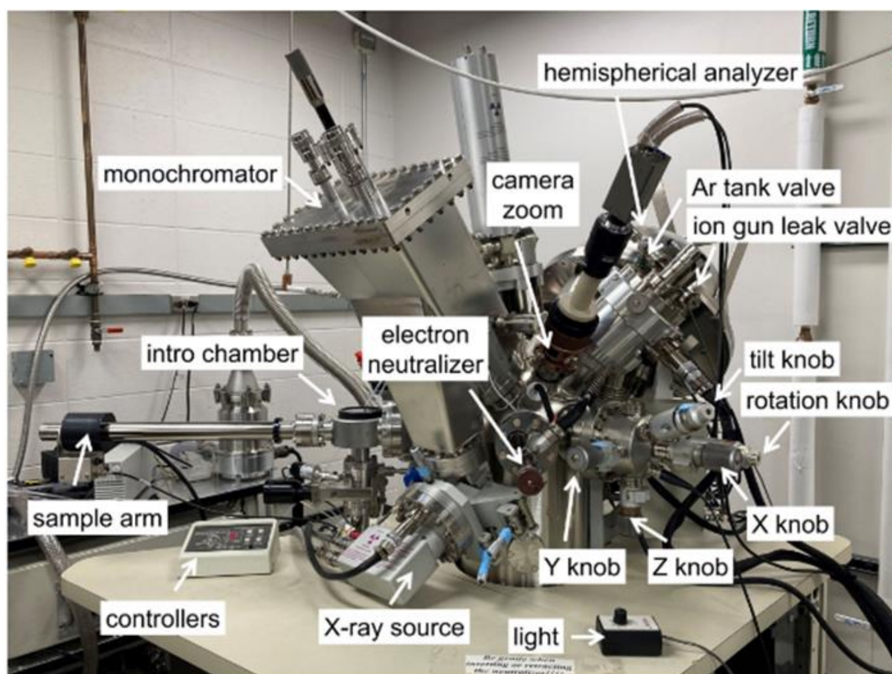

Figure 23 Picture of the XPS system at CSU.

XPS is a surface-sensitive analytical technique used to determine the elemental composition and chemical state of materials. The back surface of the CdTe film is bombarded with X-rays of a specific energy, typically generated by a monochromatic X-ray source. When these X-rays strike the surface of the sample, they eject core-level electrons from the atoms in the material. The energy of the ejected photoelectrons is characteristic of the element from which they originated and their binding energy within the material. By measuring the kinetic energies of these photoelectrons, their binding energies can be determined, providing information about the elemental composition and chemical state of the surface atoms. The instrument at CSU itself, includes a monochromatic Al kα source, hemispherical electron energy analyzer that is electrostatic in nature, a detector, and a data acquisition system that collects and processes the signal for how the sample and instrument is set up. Appropriate and careful analysis of the XPS data is crucial to make meaningful quantifications of the photoelectron signal for various elements [41]. This is achieved by making 4 corrections to the collected data as follows:

1. Relative sensitivity factors (RSFs)/Schofield cross-sections: The intensity of the detected photoelectron signal depends not only on the concentration of the element of interest but also on the probability of photoelectron emission for that element. Since the probability of photoelectron emission varies among different elements due to differences in their ionization cross-sections and other factors, RSFs are employed to normalize the detected intensities. RSFs are typically experimentally determined by measuring the XPS signal intensities from known standards containing different elements in known concentrations. By comparing the measured intensities to the known concentrations, RSFs can be calculated for each element and chemical state. These factors are usually expressed as ratios relative to a reference element, often carbon (C1s), whose RSF is defined as 1.0.

2. Angular distribution correction: This is the correction of how the signal is collected with respect to the angle between the X-ray primary beam being impacted on the sample and the angle between the photoelectrons that are ejected and the hemispherical analyzer.

3. Transmission function: This refers to the efficiency with which emitted photoelectrons are transmitted through the various components of the instrument, including the sample, analyzer, and detector, before being detected. It represents the probability that a photoelectron emitted from the sample will successfully reach the detector and be registered as a signal.

4. Escape depth correction: Emitted photoelectrons do not always escape directly from the surface of the material. Some photoelectrons may undergo inelastic scattering events or interactions with neighboring atoms before finally escaping the material.

As a result, the kinetic energy of the emitted photoelectrons may be lower than expected based solely on the binding energy of the core-level electrons from which they originated.

Chapter 4: HYPOTHESIS 1

4.1 Background to hypothesis 1

Since As is a promising pathway to improving voltage, and it is established that a Cd overpressure is required to incorporate arsenic effectively, Cd_3As_2 was selected as the doping source charge. It was thought to be a best of both worlds option, where the Cd would provide the required overpressure for the As to be incorporated and ionized [30]. However, Cd_3As_2 is a 3-dimensional semi-metal. A semi-metal has unique electronic properties that may seem attractive in photovoltaic and optoelectronic applications, but the interaction of this material with CdTe is unknown[nature ref]. Hence, to avoid a convolution during this investigation, it was thought to anneal the px-CdTe thin films over a source of Cd_3As_2. This means that Cd_3As_2 is not deposited on the surface of CdTe and As species diffuses into the film. Hence, *the first hypothesis states that As can be incorporated into CdTe using Cd_3As_2 without depositing its film*. The most effective way to prove/disprove this hypothesis was to characterize films with SIMS, to analyze the concentration at the back surface and within the film, and with XPS, to analyze the surface of the film.

4.2 Device fabrication and analysis for hypothesis 1

4.2.1 Device fabrication for SIMS analysis

A 3.6 µm film of $CdSe_xTe_{1-x}$ (x=0.4) was deposited onto MZO and FTO on TEC10 glass in the ARDS. The 100 nm MZO film was deposited using RF sputtering. However, for such a thick film of $CdSe_xTe_{1-x}$, the superstrate heater in the ARDS requires higher temperature for the film quality at the surface to be of a good quality. Hence, the superstrate heater was heated to a temperature of 500℃, as opposed to the temperature of 420℃ when depositing both, $CdSe_xTe_{1-x}$ and CdTe. Vacuum was broken post deposition and the sample moved to the HBJ for the Cd_3As_2 treatment. The Cd_3As_2 treatment was carried out at

1Torr under Argon as the operating vacuum and the superstrate heater was kept hotter (500°C) than the source heater that contained Cd_3As_2 (355°C). The selection of the source heater temperature was based on the vapor pressure data of Cd_3As_2 [42]. The sample was allowed to cool in vacuum of the HBJ following the cadmium arsenide treatment to maintain the integrity of the glass. The device structure can be seen in Figure 24. SIMS analysis was performed at Eurofins EAG laboratory and the concentration of As was measured as a function of the $CdSe_xTe_{1-x}$ film depth.

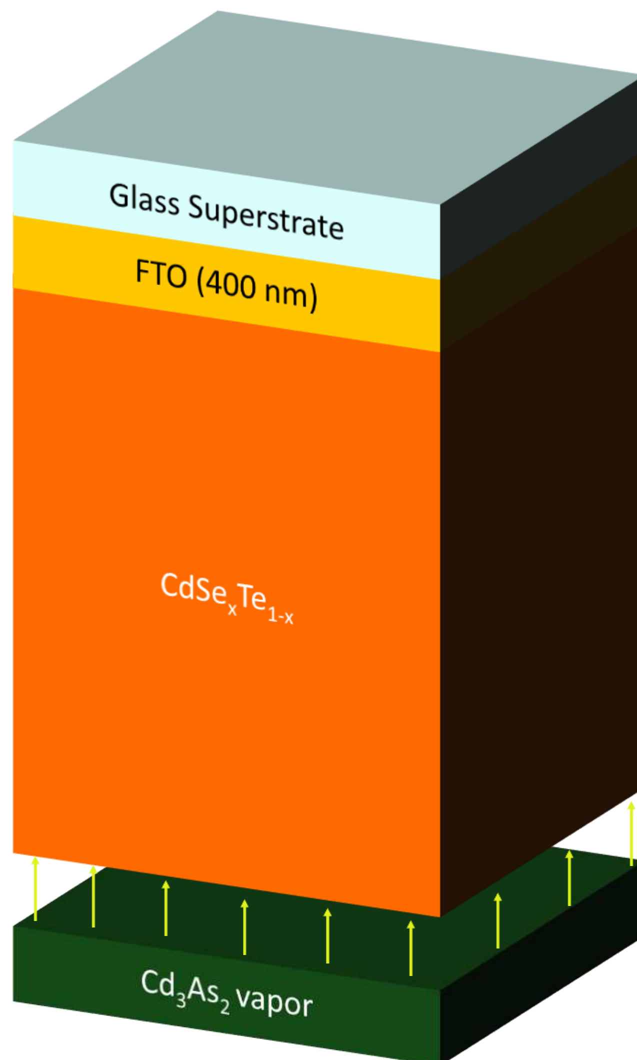

Figure 24 Device structure for SIMS analysis.

4.2.2 SIMS Analysis

The concentration of As measured by SIMS showed a typical diffusion behavior, as seen in Figure 25. The concentration of As near the back surface of the film is ~10^{20} atoms/cc^{-1}, drops as a function of film depth down to 0.5 µm, but then picks up from 0.5 µm to 0.1 µm. Notably, the concentration at the back surface of CdTe is not high enough to be considered a monolayer or a material that has formed a bulk. For a solid atomic species to be considered as a bulk, the concentration of atoms should be on the

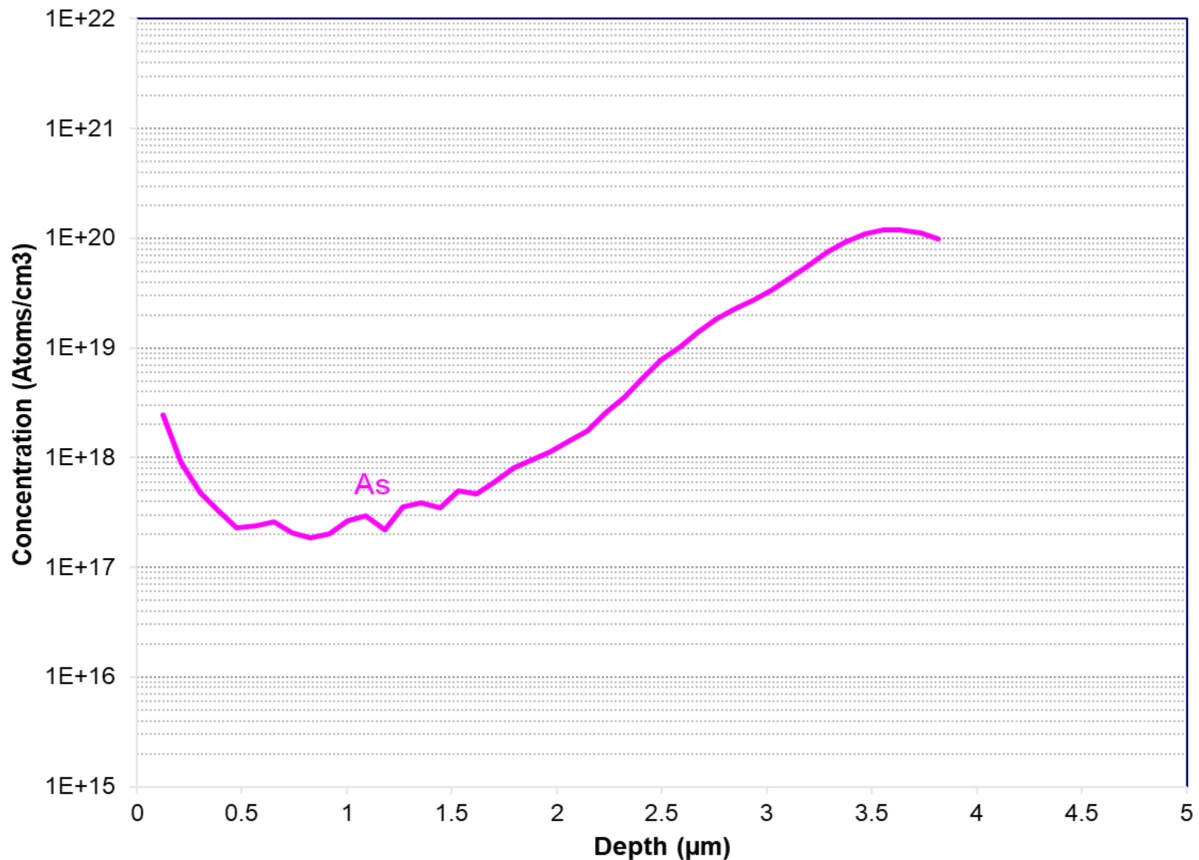

Figure 25 Concentration profile of As as a function of film depth following the Cd3As2 treatment in the HBJ.

order of 10^{22} or 10^{23} atoms/cc^{-1}. This fact arises from a simple calculation considering molar volume and the Avogadro number.

From the SIMS plot in Figure 25, the increase in concentration observed right at MZO interfacing with $CdSe_xTe_{1-x}$ is unusual and could either indicate interdiffusion of As with an atomic species in the MZO window layer, or a more likely explanation is that the MZO film itself carrier an impurity of As.

4.2.3 Device fabrication for XPS analysis

Since XPS gives information about the bonding environment of elements at the surface, it was important to establish a reference of what photoelectron signals of Cd and As from a Cd_3As_2 bulk surface look like.

Sample no. 1 was the reference Cd_3As_2 film deposited on TEC10 glass with FTO, in the HBJ with the superstrate source temperature colder, at 300°C, than the bottom source heater containing Cd_3As_2, at 400°C and for 20 minutes.

Sample no. 2 was a $CdSe_xTe_{1-x}$ and CdTe bilayer film deposited on to TEC10 glass with FTO and a 100 nm MZO layer that was deposited using RF sputtering. The deposition of $CdSe_xTe_{1-x}$ and CdTe was carried out in the ARDS, with the top superstrate source temperature at 420°C and 500°C, respectively, and the source temperature at 575°C and 555°C respectively. The film thickness was ~3.5 µm. The sample was then placed in the HBJ by breaking vacuum from the ARDS, for the Cd_3As_2 annealing treatment where the top superstrate source temperature was maintained at 500°C, and the bottom source temperature at 355°C, for 20 minutes. Both samples were allowed to cool in vacuum in the HBJ,

and following this step, were taken to the XPS measurement facility at CSU. The device structure for samples no. 1 and 2 are shown in Figure 26.

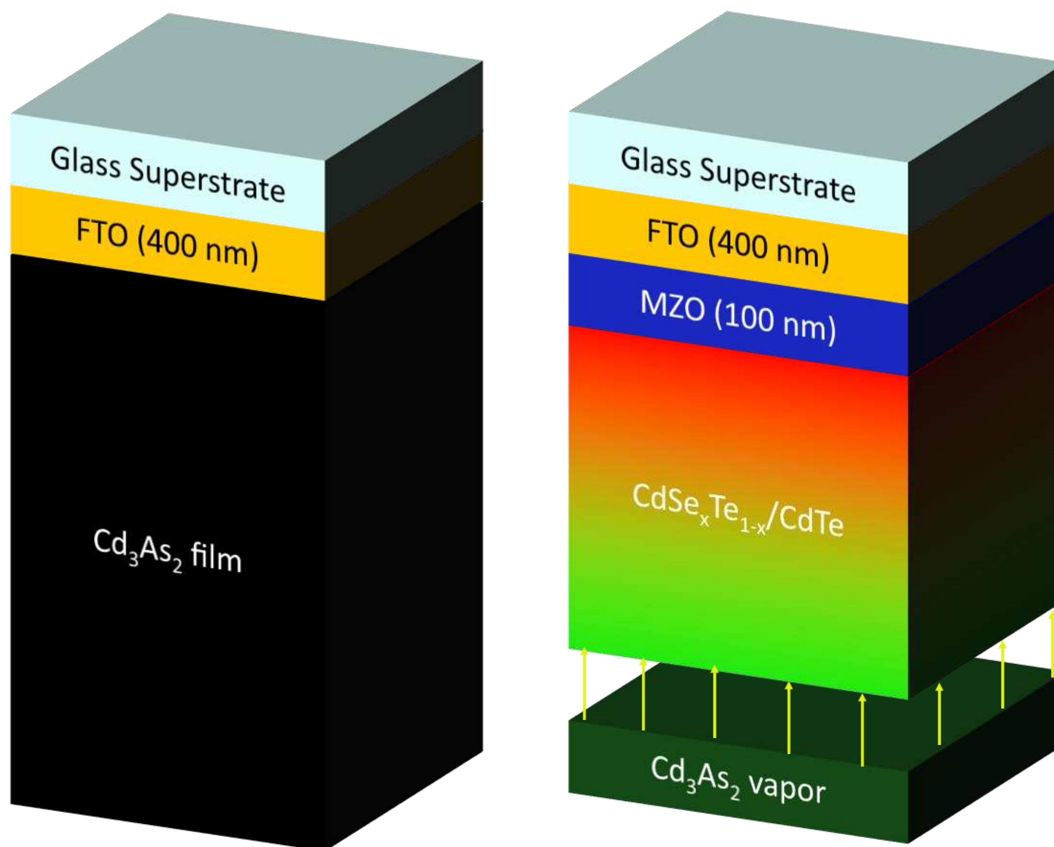

Figure 26 Left: film structure for reference sample (sample no. 1); right: film structure of Cd3As2 treated bilayer (sample no. 2)

4.2.4 XPS analysis

The XPS photoelectron spectra analysis was carried out expecting to get a quantification. First, a survey spectrum was acquired to understand a rough estimate of the concentration of elements in both samples, by observing intensities of each photoelectron signal. Following this, a high-resolution spectrum for all elements expected to be significant in concentration were acquired. These elements included Cd, Te, Se, As, O and C. These elements were scanned in the range of 3d, 3d, 3d, 1s and 1s binding energies of their orbitals, respectively. The element of interest to work on the hypothesis was As in the 3d orbital binding energy range. However, upon further investigation, it was found that As 3d overlaps with Te 4d orbital binding energy and convolutes the spectra, making it too complex to analyze

effectively. Hence, for sample no. 2, As was scanned in the 2p orbital range, as opposed to sample no. 1, where As was scanned in the 3d orbital range.

However, As in the 2p orbital has no known RSFs and quantification without this information is not possible. Hence, to estimate whether a film of Cd_3As_2 was deposited on sample no. 2, the signal to noise ratio (S/N) was observed.

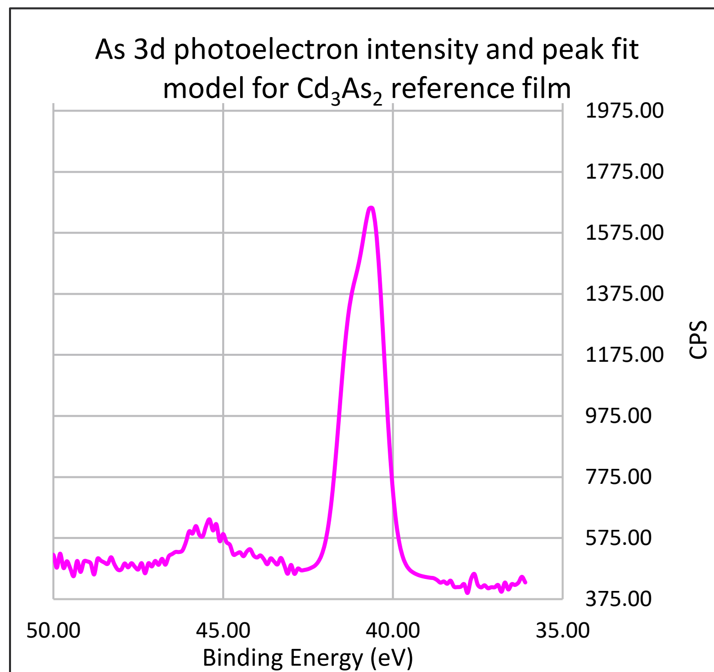

Figure 27 As 3d photoelectron spectra from reference sample (sample no. 1)

The signal to noise ratio gives qualitative information about the concentration of As. Meaning, if the photoelectron signal is clean without noisy background, it can be considered that the element in question is in high concentration, where high concentration is subjective. Comparing the photoelectron intensities and S/N for As in the 3d orbital for the reference sample (sample no. 1), and for As in the 2p orbital for the bilayer sample annealed over Cd_3As_2 (sample no. 2), which can be seen in Figures 27 and 28 respectively, the conclusion is that As is in lower concentration in sample no. 2. This cross-verifies the

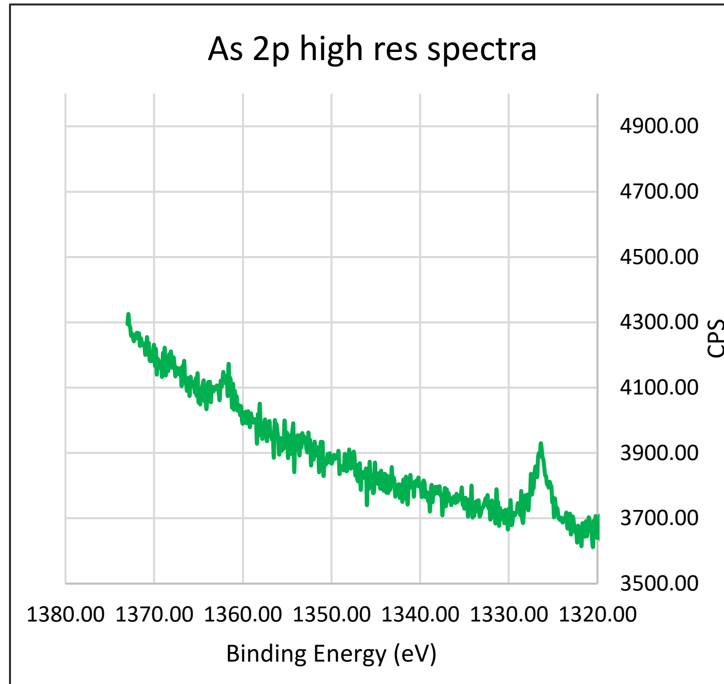

Figure 28 As 2p photoelectron spectra from bilayer sample annealed over Cd3As2 (sample no. 2)

concentration of As acquired from SIMS, and hence hypothesis 1 is *proven* and that As is incorporated into the film.

4.2 Diffusion of As in $CdSe_xTe_{1-x}$

Due to the SIMS data that was acquired for As concentration, it was helpful to compare the diffusion of As and Cu in Cd(Se)Te thin films. The SIMS data for a Cu doped bilayer sample had already been acquired prior to starting this investigation. Now, a diffusion fit was created from this data and the diffusivities of both dopants were calculated.

Firstly, to analyze the diffusion coefficient of As and Cu, the SIMS data was fitted in MATLAB using a least squares curve fit method. Equation (4) is used to fit the SIMS data of Cu, as taken with reference to [27]. Equation (5) is used to fit the SIMS data of As, as referenced from [43]. The parameters $c(x,t), c0, c_{s0}, c_{f0}, x, D, D_s, D_f, t$ represent concentration as a function of position (depth) and time, initial concentration, initial concentration of the slow diffusion, initial concentration of the fast diffusion,

position (depth), diffusivity, slow diffusivity, fast diffusivity and time, respectively. An initial guess of the unknown values D, D_s, D_f with reasonable upper and lower limits of the same was taken. The values of c_{s0} and c_{f0} are unknown as well. However, the purpose of this study is to obtain the diffusivities described above.

$$c(x,t) = c_s * erfc\left(\frac{x}{2\sqrt{D_s t}}\right) + c_f * erfc\left(\frac{x}{2\sqrt{D_f t}}\right) \quad (4)$$

$$c(x,t) = c_0 * erfc\left(\frac{x}{2\sqrt{Dt}}\right) \quad (5)$$

From the diffusion fits of the models described above in equations (4) and (5) and shown in Figure 29, the diffusivities are reported as:

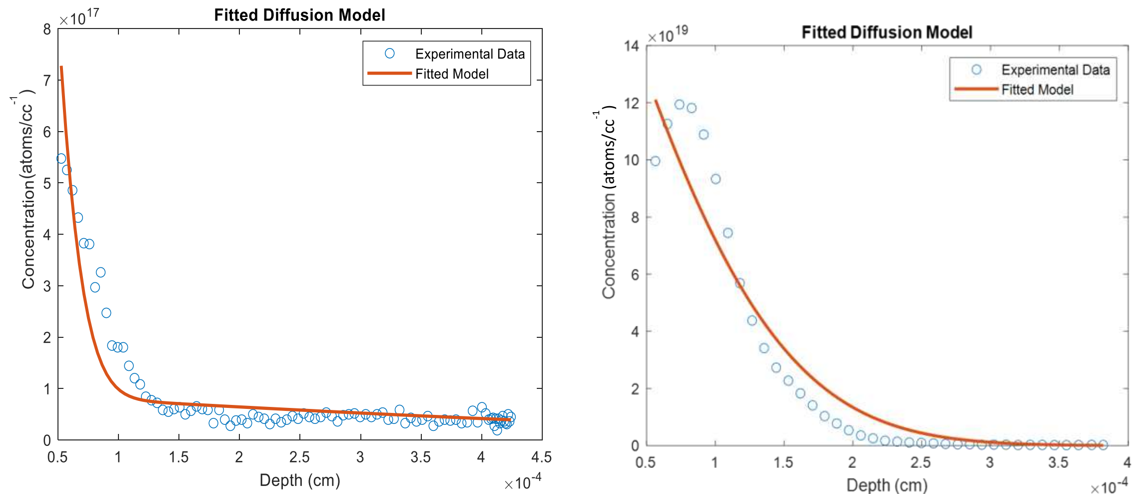

Figure 29 Fitted diffusion models for Cu (left) and As (right) as a function of film depth and time.

- *Fitted Df(cm²/sec) for Cu: 1.8245*10⁻¹⁰*
- *Fitted Ds(cm²/sec) for Cu: 7.6493*10⁻¹³*
- *Fitted Diffusion Coefficient for Arsenic (D)(cm²/sec): 3.3109*10⁻¹²*

Jones et al [27] note that Cu has a fast and slow diffusing component, with the fast component attributed to grain boundary diffusion and the slow, to intragrain diffusion. This fact is confirmed with the data fitting of Cu concentration in the bilayer sample. Interestingly, As does not seem to have a second component or has one that is not or cannot be observed. Moreover, the diffusivity of As is slower than the slow/intragrain component of Cu by an order of magnitude. The mechanism of doping the

absorber with Cd_3As_2, to the best assumption of the author, is that the material in the source during the Cd_3As_2 treatment dissociates, adsorbs on the back surface, dissociates again, and diffuses into the film. The dominant diffusion pathway of arsenic is thought to be a combination of grain boundary and intragrain diffusion, as is common with most species' diffusion into a polycrystalline matrix [43].

Chapter 5: HYPOTHESIS 2

5.1 Background to Hypothesis 2

It has been established that in addition to doping, passivation of the back surface of CdTe is critical to improving the voltage and mitigating recombination of charged carriers. At CSU, this surface passivation was previously done by sputtering a 5 nm layer of TeO_2 on the back surface of CdTe and doping the film with As. These results were encouraging and showed a modest improvement in the V_{oc}, (Figure 30).

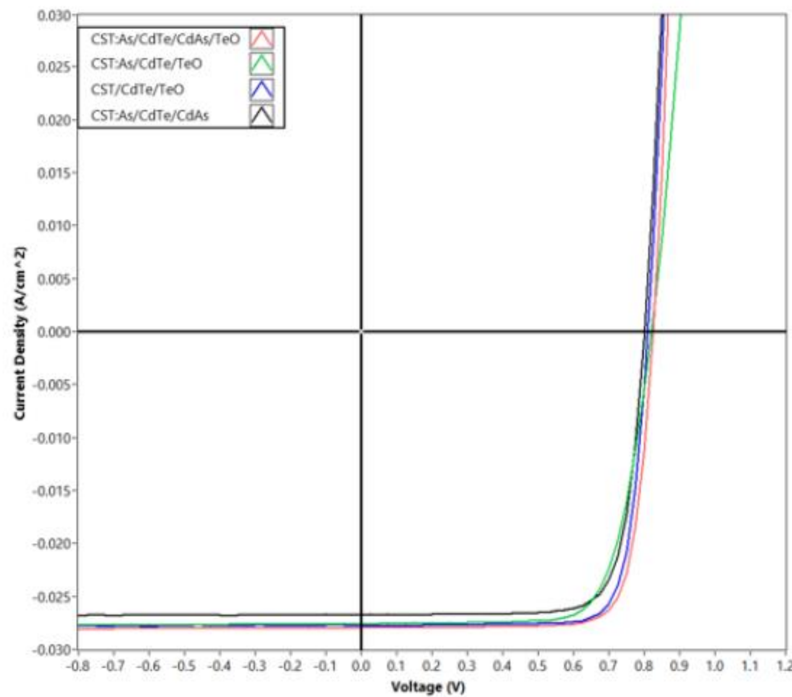

Sample	V_{oc}(mV)	J_{sc}(mA/cm^2)	FF(%)	Efficiency(%)
CST:As/CdTe/Cd_3As_2/TeO_x	825	28.0	79.6	18.37
CST:As/CdTe/TeO_x	821	27.6	73.4	16.61
CST/CdTe/TeO_x	811	27.8	80.1	18.04
CST:As/CdTe/Cd_3As_2	802	26.8	77.8	16.70

Figure 30 J-V curves and device parameters of As doped CdTe devices with two doping pathways and sputtered TeOX, by Zachary Lustig, [29].

In addition to this, it has also been established that TeO_2 can form natively (n-TeO_2), but the mechanism by which this occurs is not fully known or understood and it is estimated that this n-TeO_2 can form on a timescale of days to weeks.

However, during the course of this work, a novel process to form TeO_2 on a timescale of seconds, was developed. This process was performed in the HBJ, with and without Cd_3As_2 treatment by annealing the sample to an average high temperature of 500℃ and venting the HBJ to ambient air at those high temperatures, followed by cooling the sample in ambient air to maintain glass superstrate integrity.

The samples that had undergone this treatment gave a sharp increase in photoluminescence, indicating that something at the surface of the CdTe film was modified. The suspicion was that by exposing the sample to ambient air at high temperatures, a layer of TeO_2 had been formed. Hence, hypothesis 2 states that *exposing a CdTe film to ambient air at high temperatures can lead to the formation of* TeO_2.

5.2 Device fabrication and structure for hypothesis 2

A control sample was fabricated by depositing a bilayer film of $CdSe_xTe_{1-x}$ and CdTe, 3.5 µm thick in the ARDS at temperatures mentioned in section 3.4, after which vacuum was broken from the ARDS and it was treated with Cd_3As_2 in the HBJ at temperatures mentioned in chapter 4 for this treatment and allowed to *cool in vacuum*. This control sample was then treated with $CdCl_2$ to passivate the grain boundaries and promote grain growth. Finally, it was exposed to ambient air at *room temperature* for a week.

The second sample has identical film structure and Cd_3As_2 treatment, but following the Cd_3As_2 treatment, was exposed to ambient air at the high temperature and allowed to cool in ambient air, while still placed in the HBJ. Following this step, a the $CdCl_2$ passivation treatment was done in the ARDS. This

sample was prepared within the 1 week that the control sample was exposed to room temperature

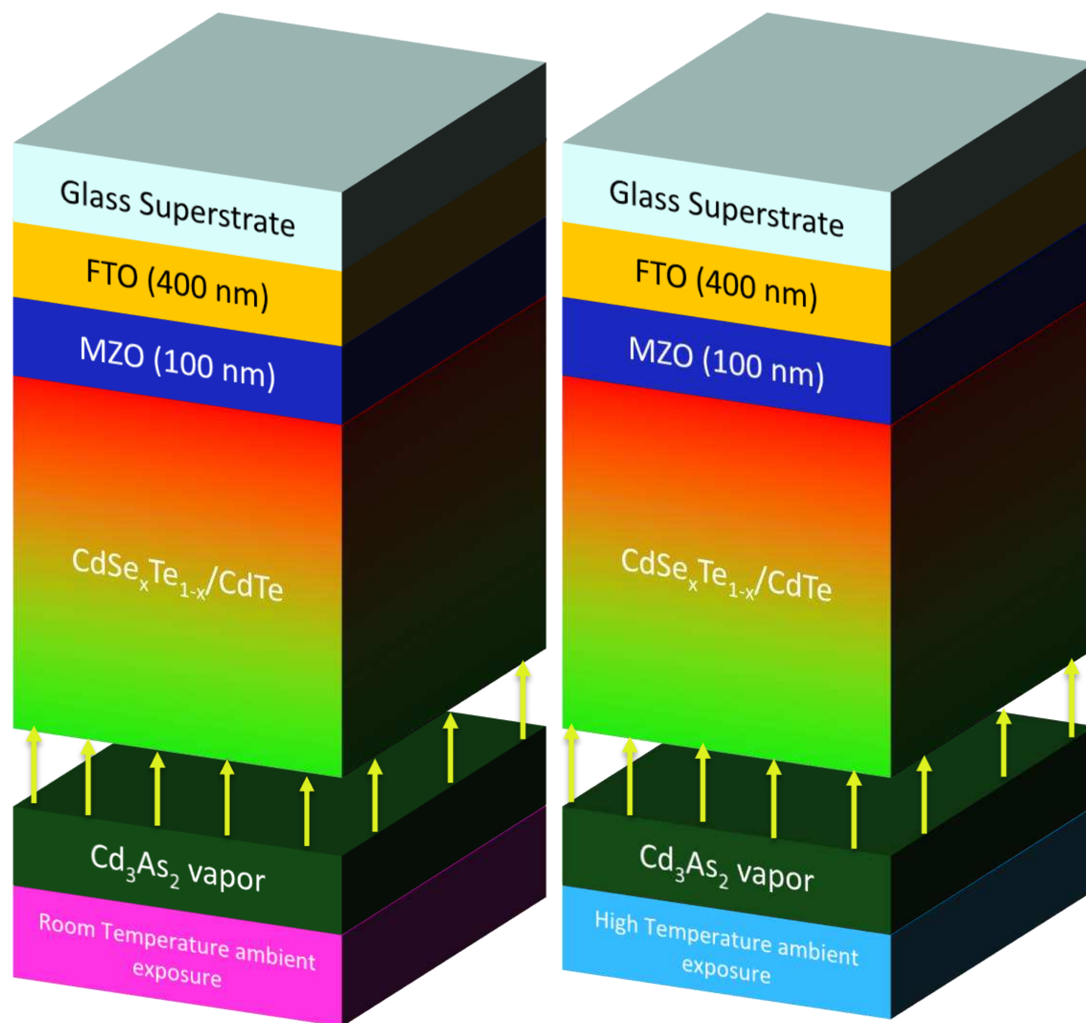

Figure 31 Film architecture; left: control sample exposed to ambient air at room temperature, right: sample exposed to ambient air at high temperature post Cd3As2 treatment in the HBJ.

ambient air for. The film architecture for these two samples is shown in Figure 31.

Both samples were taken to the XPS facility at CSU and the back surfaces were characterized and the element stoichiometry was quantified.

5.3 XPS analysis of samples for hypothesis 2

High resolution spectra for both samples were taken for Cd, Te, Se, O, C in the binding energy range for the orbitals 3d, 3d, 3d, 1s, and 1s respectively. It was noted that the Te 3d photoelectron signal

had a distinguished peak besides the primary Te 3d 3/2 and 5/2 binding energy peak locations, for both of the samples. The quantification of this data was carried out for Te and O in the following manner.

- Using the CasaXPS software for spectrum analysis.
- Creating regions for Te 3d 5/2 and O 1s peaks with sufficient background information.
- Using the ADC to account for changes in the RSF.
- Fitting the background with the Tougaard method to account for inelastic scattering of electrons.
- Fitting the peaks with a Lorentzian lineshape to account for all features within the area enclosed by the peaks.
- Calculation of the area under the curve for each peak fit was performed by the CasaXPS software to output the stoichiometry.

Figure 32 (a), (b) shows the XPS spectra of Te 3d and O 1s respectively, for the reference sample exposed to ambient air for a week.

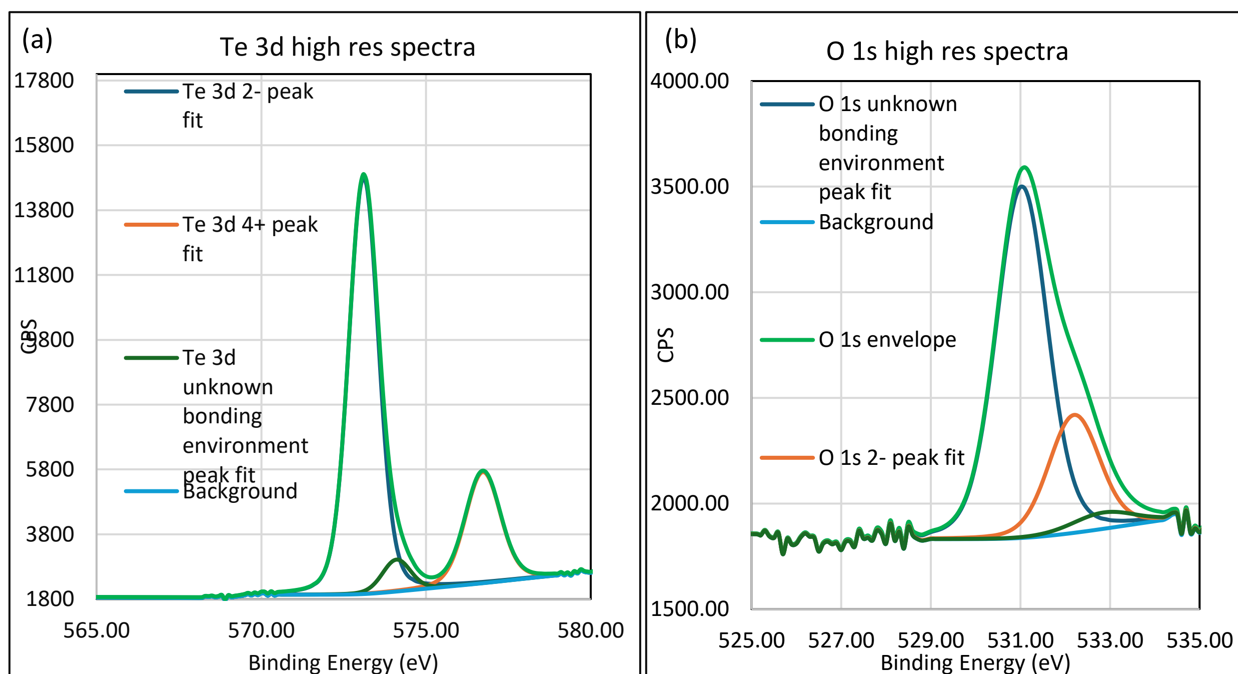

Figure 32 XPS spectra of (a) Te 3d and (b) O 1s spectra in sample where TeO2 was formed at ambient conditions.

Figure 33 (a), (b) shows the XPS spectra of Te 3d and O1s for the sample that had undergone the vacuum anneal/Cd3As2 treatment in the HBJ and exposed to ambient air rapidly, by venting the HBJ.

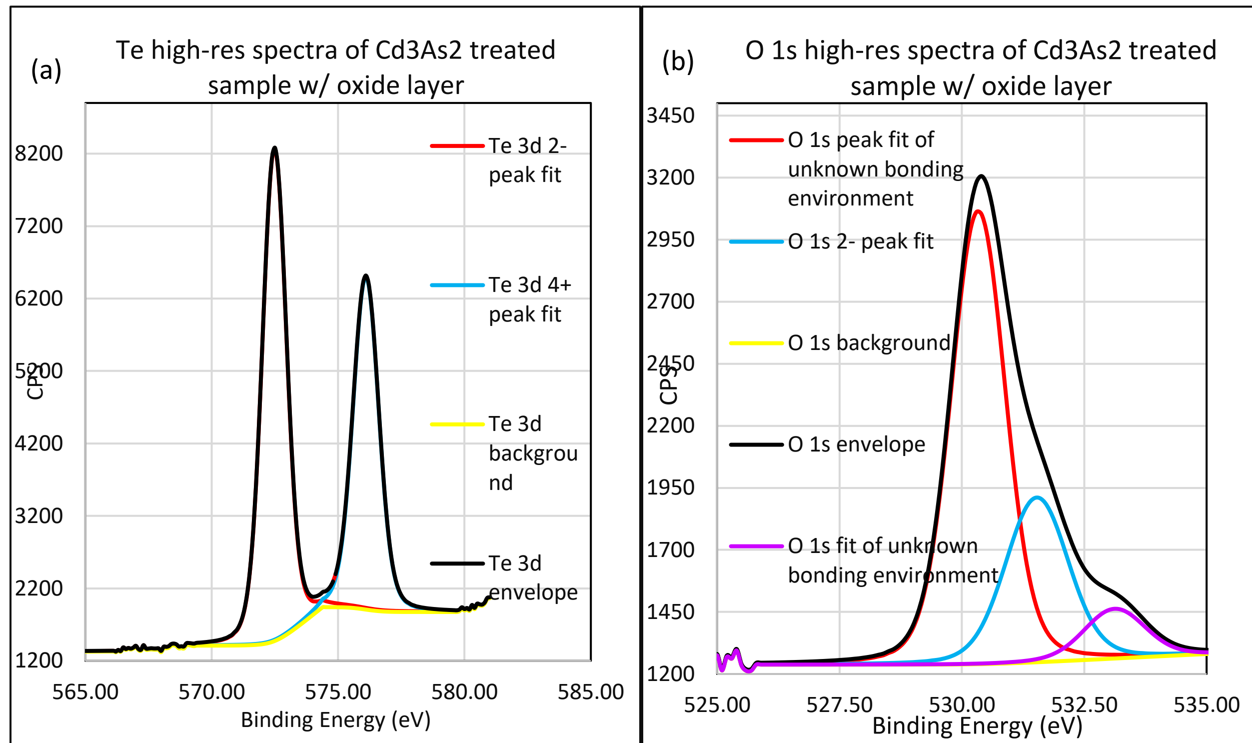

Figure 33 XPS spectra of (a) Te 3d and (b) O 1s spectra in sample where TeO2 was formed by exposing sample to ambient air at high temperature.

The key point to note is that the Te 3d 5/2 photoelectron signal for both samples, where Binding Energy = 572.5 has a charge of 2^- [37, 44], indicating bonding with Cd. The signal beside it is an oxide signal, with a charge of 4^+, indicating bonding with O, with binding energy of ~576.4 eV.

Analyzing O is more complex than Te, since it has distinct features underneath the envelope (shown in light green and black). The highest and lowest peak fits of oxygen signals arise due to bonding with different compounds or atoms and this bonding environment is not known. However, the oxygen peak fit signal in the middle had a stoichiometric ratio with Te of 2:1, indicating O bonding to Te with a charge state of 2^-. Additionally, the stoichiometry for CdTe resulted in a 1:1 ratio Cd:Te, indicating meaningful quantification. Thus, it is *proven that when a CdTe film is exposed to ambient air at high*

temperatures, a layer of TeO_2 is formed. For proceeding chapters, this process has been called rapid oxidation for ease of understanding.

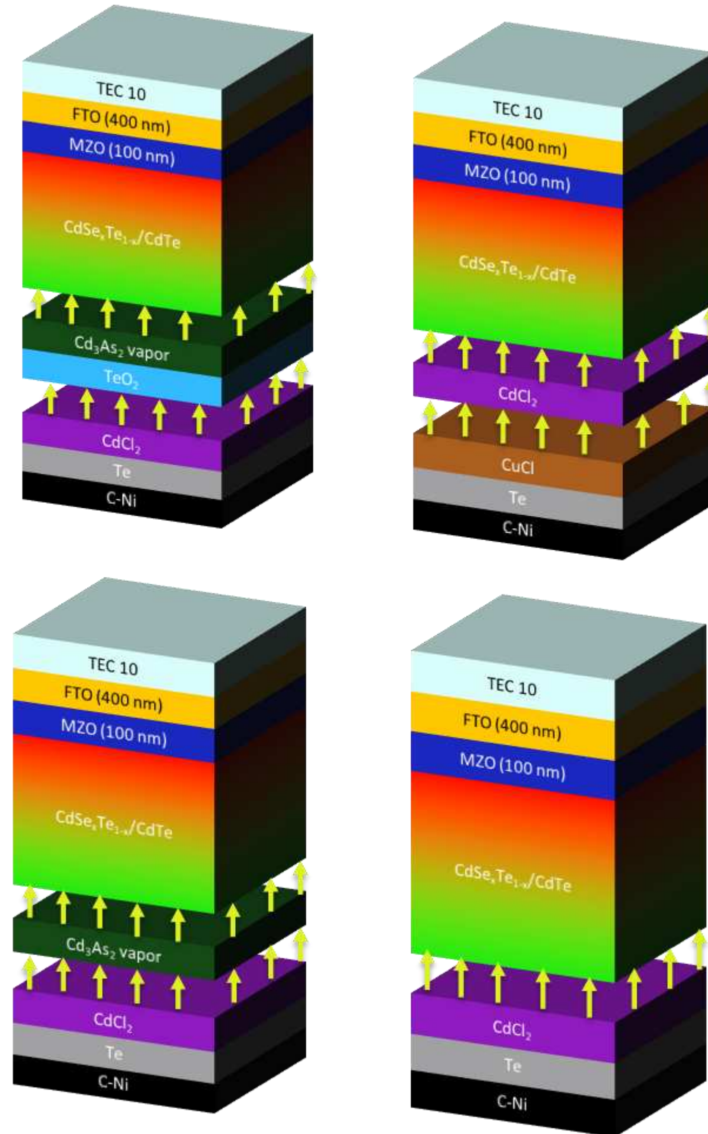

Figure 34 Film structure for Photoluminescence measurements.

5.4 Photoluminescence of CdTe with TeO_2 formed by novel method.

As stated in section 5.1, the samples that had undergone this novel process of forming TeO_2 demonstrated a sharp improvement in photoluminescence. To isolate the effect of TeO_2, photoluminescence of 4 distinct film structures was measured. These film structures are shown in Figure 34.

The photoluminescence shown in Figure 35 demonstrates drastic improvement with the addition of the TeO_2 layer by rapid oxidation. Such a drastic improvement in the PL needs further investigation, as higher PL implies higher carrier lifetimes.

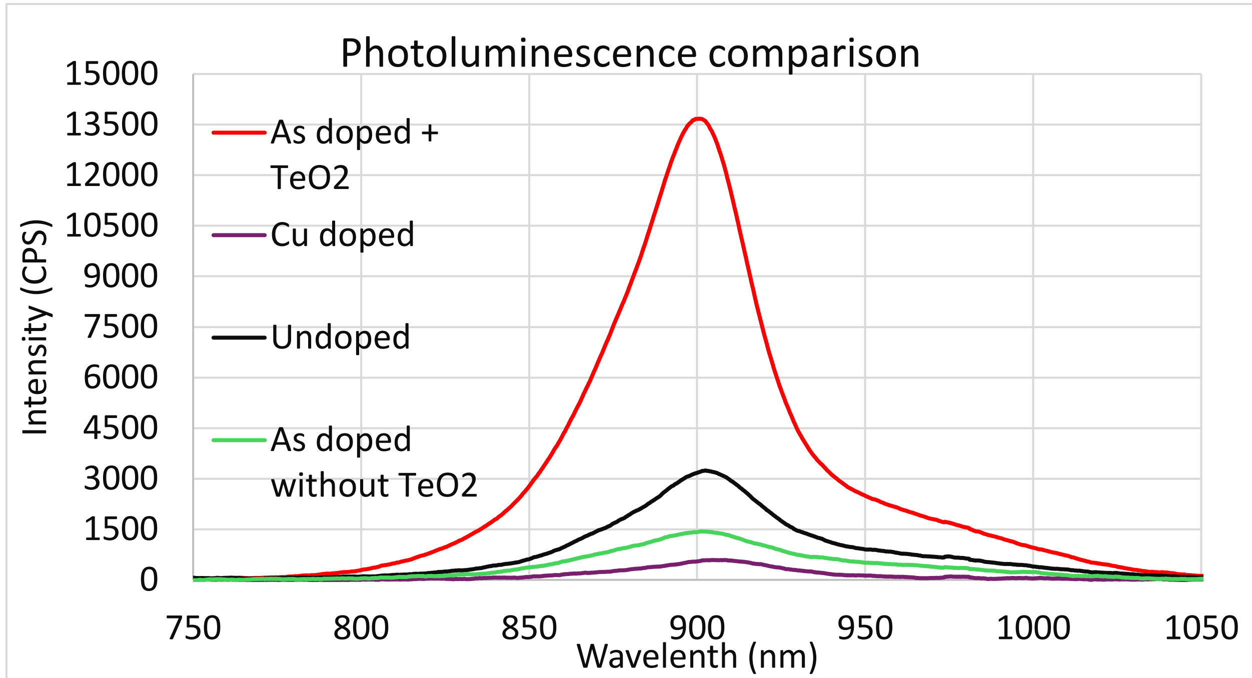

Figure 35 Photoluminescence of Cu doped, As doped, As doped with TeO2 and undoped samples.

5.5 Electrical characterization of devices with various doping treatments and TeO_2

Naturally, with such an improvement to the PL, characterization of electrical characteristics was obligatory. Hence, the samples with the film structure shown in Figure 34 were completed by depositing a 30 nm layer of Te, C-Ni paint, delineated into 25 small area cells on each superstrate and characterized at the J-V tester. The J-V curves for the best performing cells among these samples are shown in Figure 36. In the As doped sample that did not have a layer of TeO_2 by rapid oxidation, a 'kink' in the J-V curve was noticeable for nearly 90% of the cells, and in the sample that did have TeO_2, the kink was present in

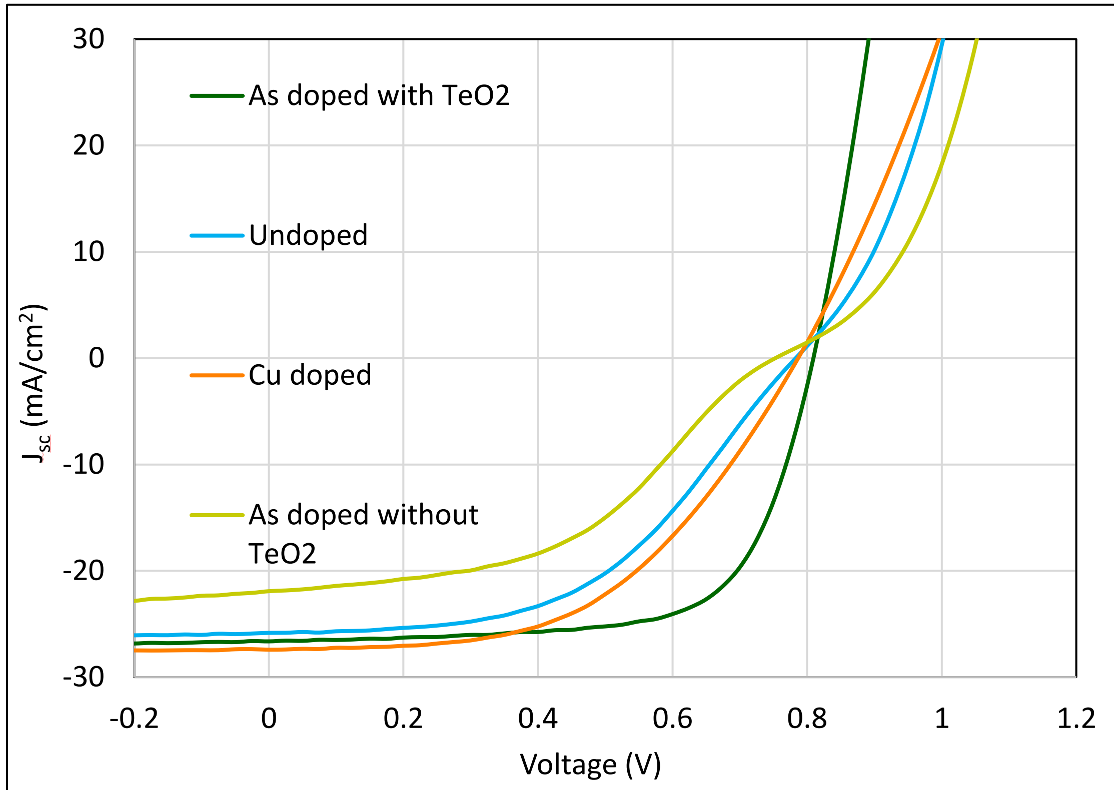

Figure 36 J-V curves of best performing cells with film architecture shown in figure 33.

50% of the cells. This kink indicates that the carriers are experiencing a barrier, cannot be extracted into the connected external circuit of the J-V tester, also limit the V_{oc} and hence, the device performance.

Intuitively, a mild dose of Cu was introduced in an As doped sample that was fabricated next *after* the $CdCl_2$ treatment, which was followed by forming the TeO_2 by rapid oxidation. This mild Cu doping was done to reduce the resistance or barrier experienced by the carriers. As a result, a cell with

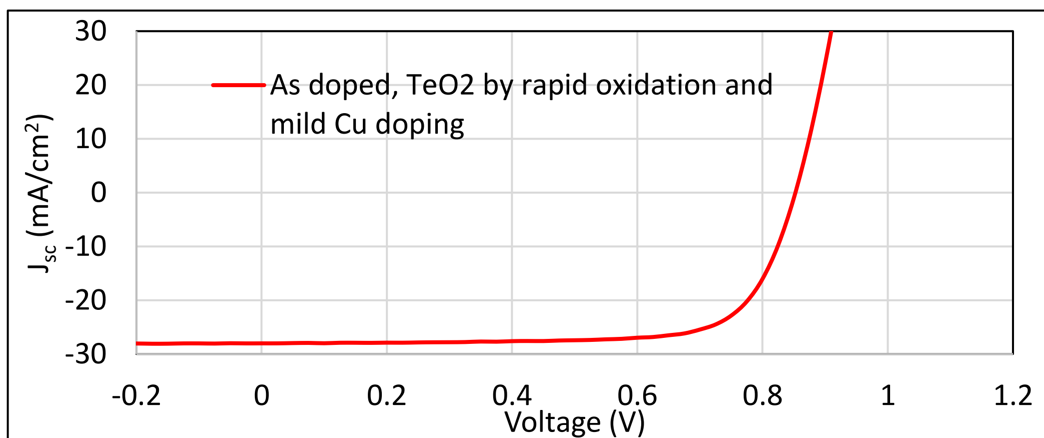

Figure 37 J-V curve of 18% efficient cell.

nearly 18% power conversion efficiency was measured, and the J-V plot is shown in Figure 37.

Additionally, a V_{oc} of 875 mV was recorded. This was the highest performing cell during this study.

However, it is noted that series resistance is still high, and there is room for significant improvement.

Chapter 6: HYPOTHESIS 3

6.1 Background to hypothesis 3

Even though a best performing cell of 18% efficiency and 875 mV V_{oc} was achieved, it remains at 75% of the SQ limit. The current theory from one source is that $CdSe_xTe_{1-x}$ produces a voltage deficit due to a defect in the material. This defect is associated with a vacancy of Se or Te and shows up when measuring photoluminescence. However, this defect lies within the bandgap of $CdSe_xTe_{1-x}$, which has a bandgap of 1.4 eV. The energy at which this defect is observed is at 1.1 eV, at 1100 nm, when the carriers recombine and emit a photon of this wavelength. The intensity of the PL emission for this defect is much larger than the intensity of the PL emission coming from the bandgap of $CdSe_xTe_{1-x}$ or a bilayer containing both, $CdSe_xTe_{1-x}$ and CdTe (~1.45 eV). However, substantiated evidence is very limited [45, 46]. Further, a theory was developed during this study, that As doping mitigates this by replacing the defect with an As atom and could be seen in photoluminescence. However, the emitted photon due to recombination cannot be observed by a Si detector, as the wavelength lies outside the bandgap of Si. Hence, an Indium-Gallium-Arsenide detector is utilized due to its larger bandgap. To investigate this and confirm or deny this theory, the third and final hypothesis states that *As doping using Cd_3As_2 mitigates this sub-bandgap emission in photoluminescence originating from $CdSe_xTe_{1-x}$.*

6.2 Device Structure

Bilayer $CdSe_xTe_{1-x}$/CdTe films were deposited with a thickness of 3.5 µm in the ARDS, on 100 nm sputtered MZO and 400 nm FTO on TEC10 glass. The doping and surface treatments varied, and two samples with 5 distinct film structures each were fabricated. These film structures can be observed in Figure 38.

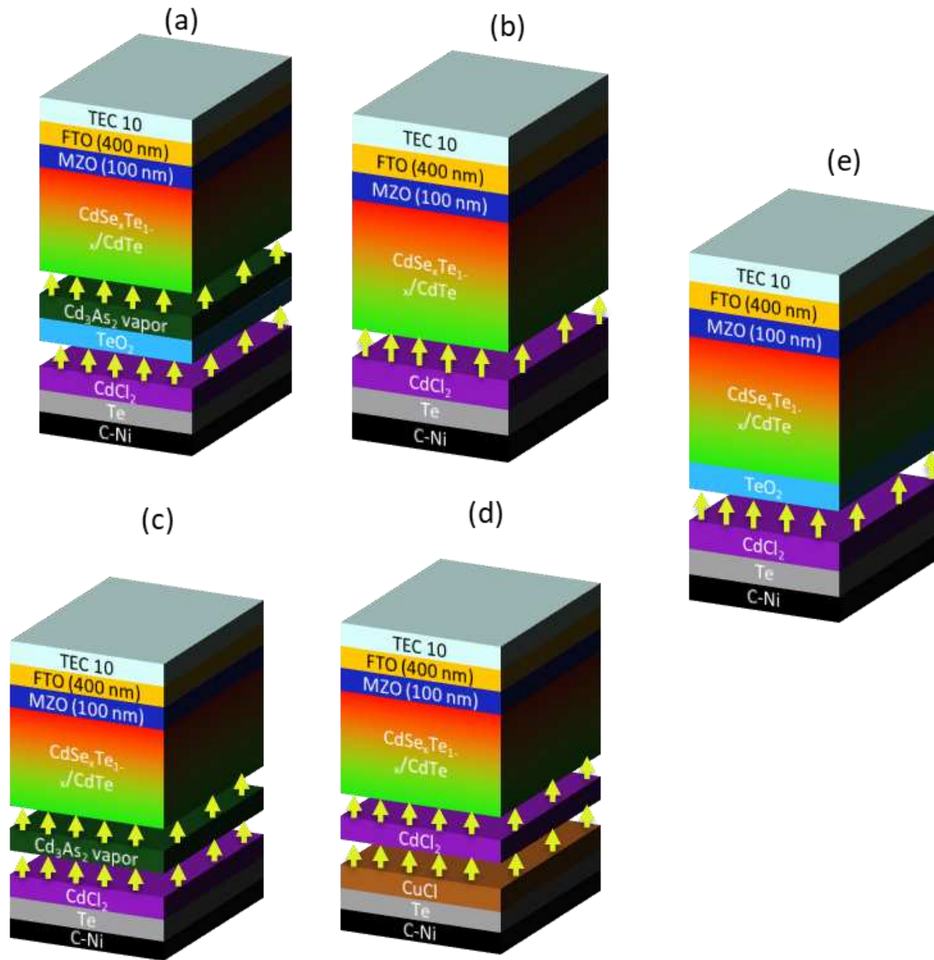

Figure 38 Various film architectures to investigate emission in photoluminescence of sub-bandgap defects.

6.3 Photoluminescence measurement

Absolute photoluminescence on the samples shown in Figure 38 was measured by Daniel Shaw.

6.3.1 Photoluminescence of As doped samples

The PL emission of As doped samples with and without TeO_2 by rapid oxidation are shown in Figure 39. Principle observation here is that there is indeed a PL emission from under the energy of the

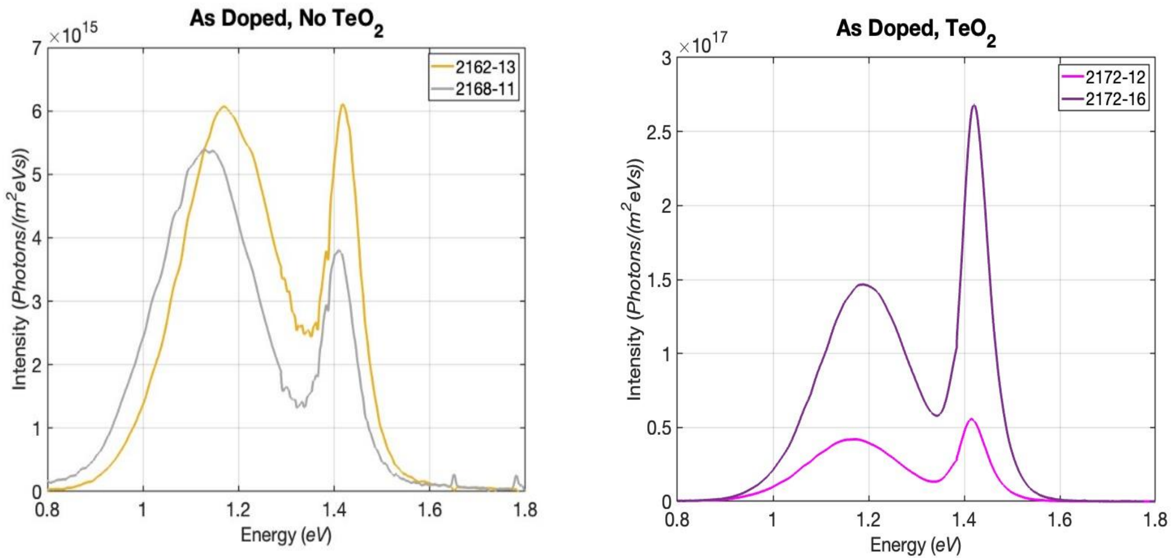

Figure 39 Absolute Photoluminescence of sub-bandgap and bandgap for As doped bilayer samples with and without TeO2.

bandgap. Hence, there could likely be a defect in the material that is causing this. Secondly, As doping without TeO_2 has no effect on the sub-bandgap defect emission in PL. However, with the addition of TeO_2 by rapid oxidation, this sub-bandgap emission is mitigated. Further, the intensity of the As doped samples without TeO_2 is 2 orders of magnitude lower than As doped samples that have TeO_2.

6.3.2 Photoluminescence of reference samples

To get a fair comparison, the photoluminescence of Cu doped and undoped samples are shown in Figure 40. In both cases, the sub-bandgap emission is just as high as the bandgap emission, and in a

similar proportion to the As doped samples without TeO_2. However, the luminescence of the undoped samples is higher by an order of magnitude.

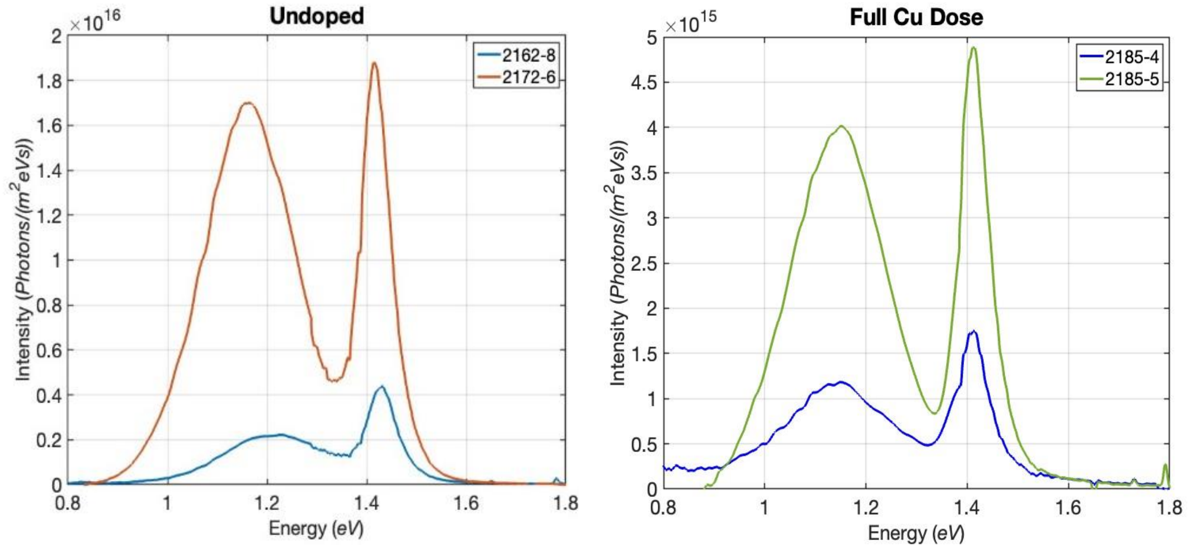

Figure 40 Photoluminescence of sub-bandgap and bandgap in Cu doped and undoped bilayer samples.

6.3.3 Photoluminescence of an undoped sample with TeO_2

From Figure 38, it is clear that As doping by itself was not lowering the sub-bandgap emission in PL. However, with the addition of TeO_2 by rapid oxidation, a sharp drop in the sub-bandgap emission was observed, as well as in the overall intensity of the PL. To isolate this effect, a sample with just the TeO_2 was fabricated as shown in Figure 38 (e) and the photoluminescence is seen in Figure 41.

From this isolated effect, it is clear evidence that TeO_2 has lowered the emission of photoluminescence originating from the sub-bandgap defect in $CdSe_xTe_{1-x}$. However, the third hypothesis only states that As doping mitigates this sub-bandgap emission in photoluminescence, and is therefore, *disproved*.

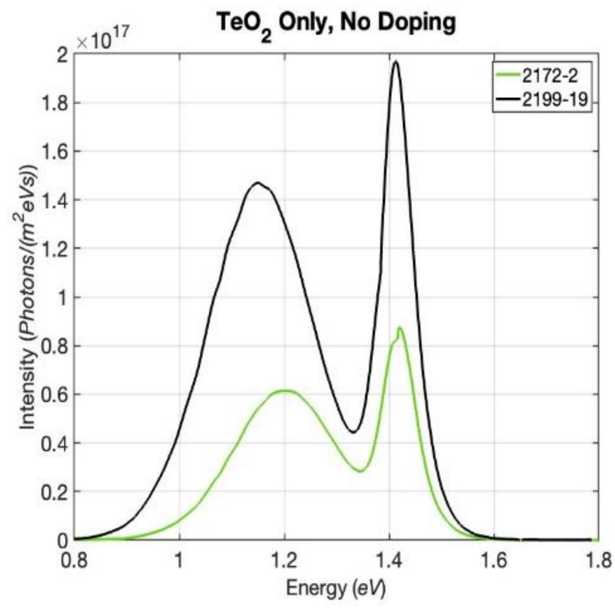

Figure 41 Photoluminescence of sub-bandgap and bandgap emissions in a sample with no intentional doping and TeO2 by rapid oxidation.

Chapter 7: DISCUSSION

In this chapter, the combined results of electrical characterization from all the experiments performed in preceding chapters are presented. The device/film structures are the same as shown in Figure 37, with a 30 nm thin film of Te and C-Ni paint applied, followed by delineating the film into 25 small area cells, contacted with In and characterized with J-V and C-V, explained in chapter 3.

7.1 J-V parameters of As doped samples without TeO_2

Here, the J-V parameters are shown in Figure 41 for the same As doped samples without TeO_2, as shown in the *J-V curve* in Figure 36.

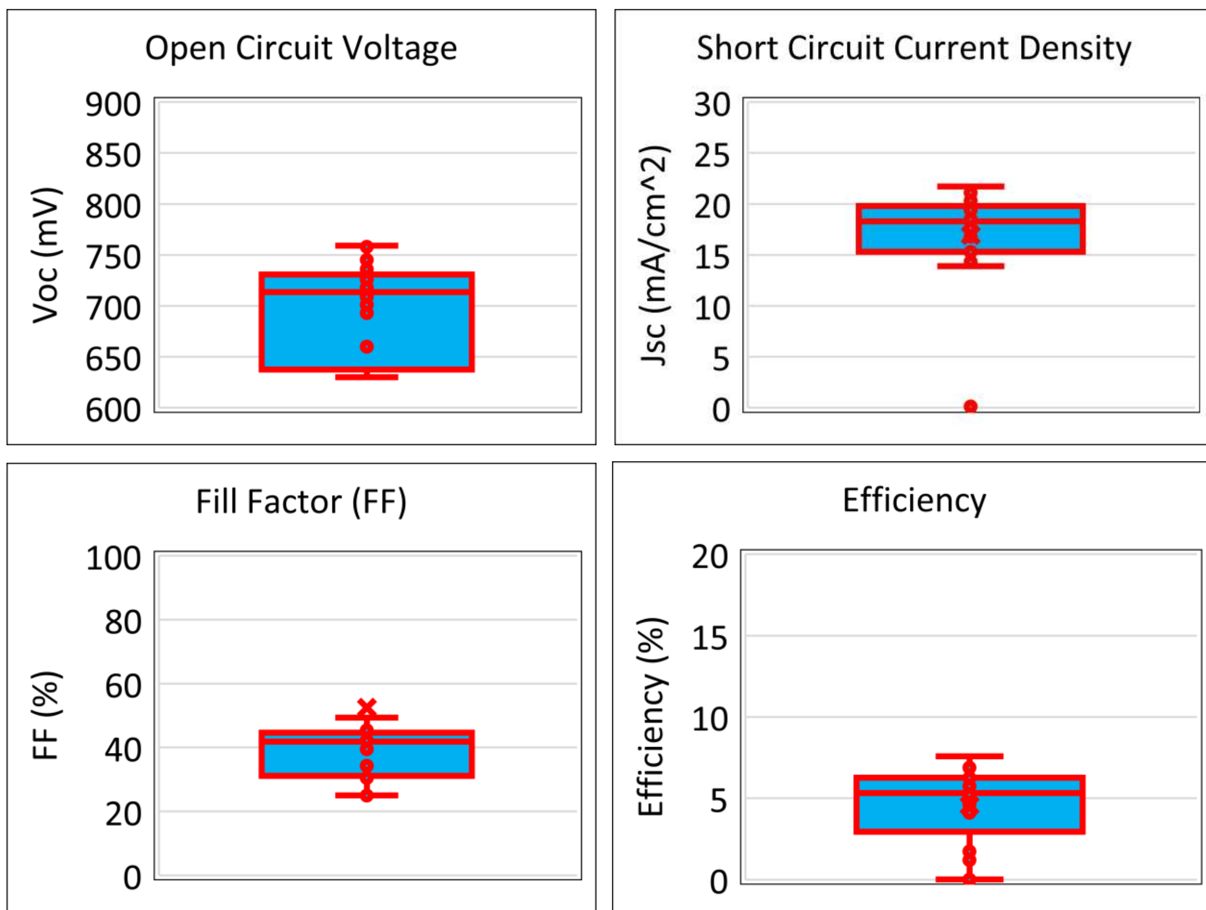

Figure 42 J-V parameters of As doped samples without TeO2.

The open circuit voltage for these cells remained underwhelming, with the highest V_{oc} being 762 mV, and a highest efficiency of 7.6%. This underwhelming performance is attributed to the presence of O_2 during the Cd_3As_2 annealing process to incorporate As. A thorough investigation is necessary to determine the effect of oxygen content during As doping processes.

7.2 J-V parameters of As doped samples with TeO_2

Now we look at the performance of bilayer samples fabricated during this study that had As doping and a layer of TeO_2 by rapid oxidation at the back surface, shown in Figure 43.

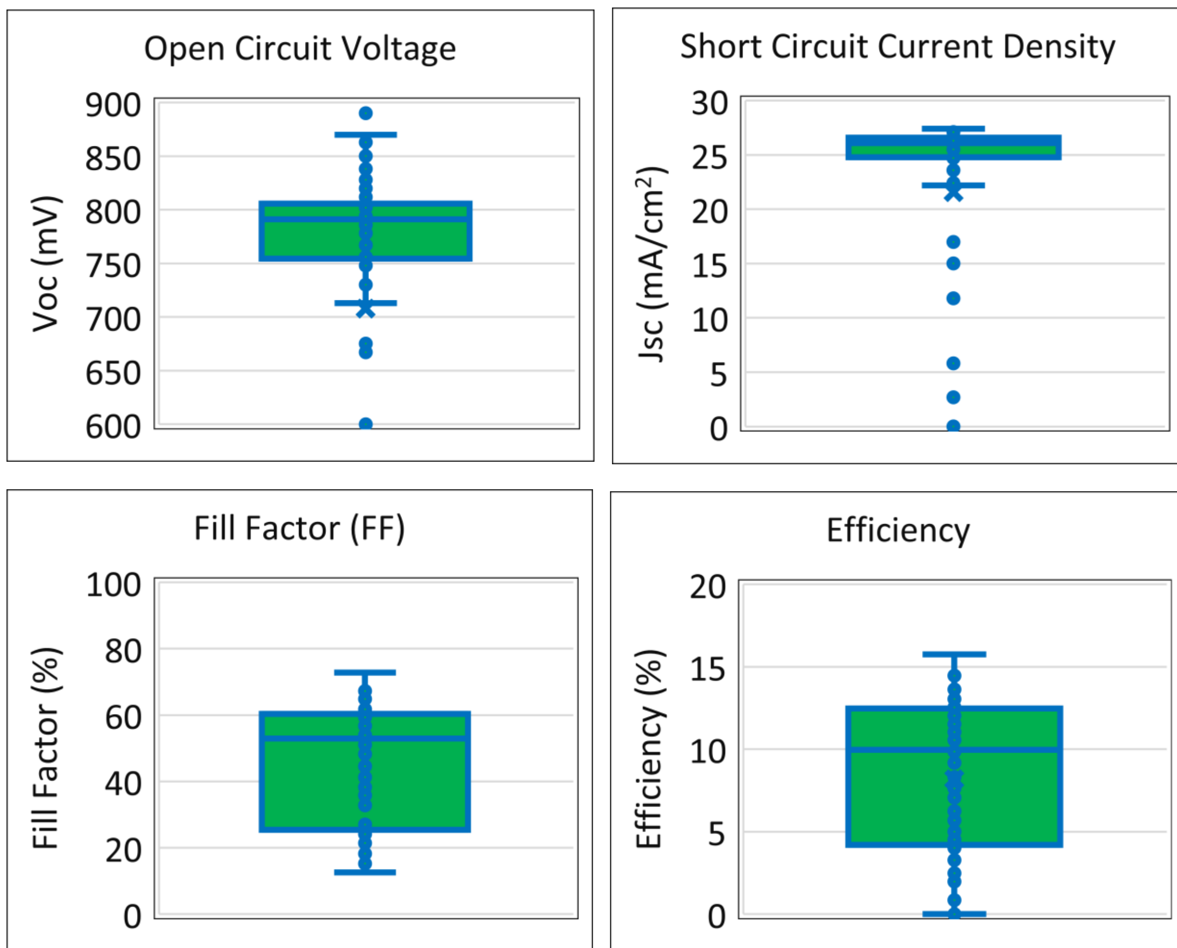

Figure 43 J-V parameters of As doped bilayer samples with TeO2 by rapid oxidation.

The V_{oc} improved drastically on these cells, with the highest one at 870 mV. However, the J_{sc} improvement was only marginally better than the As doped cells without TeO_2. This suggested there is

still some resistance to the carriers when extracting current. Hence, a mild Cu doping treatment was performed after the TeO_2 formation in later As doped samples to improve ohmic contact.

7.3 J-V parameters of As doped samples with TeO_2 with mild Cu doping

The mild Cu doping proved useful and resulted in the best performing cell in all of this study, with an efficiency of 17.84%. The V_{oc} also improved modestly by 5 mV, along with the J_{sc}, which was 28.4 mA/cm^2 at best, compared to 27.4 mA/cm^2 at best for the sample with As doping, TeO_2 and no Cu doping. The box plots for this device structure are shown in Figure 44.

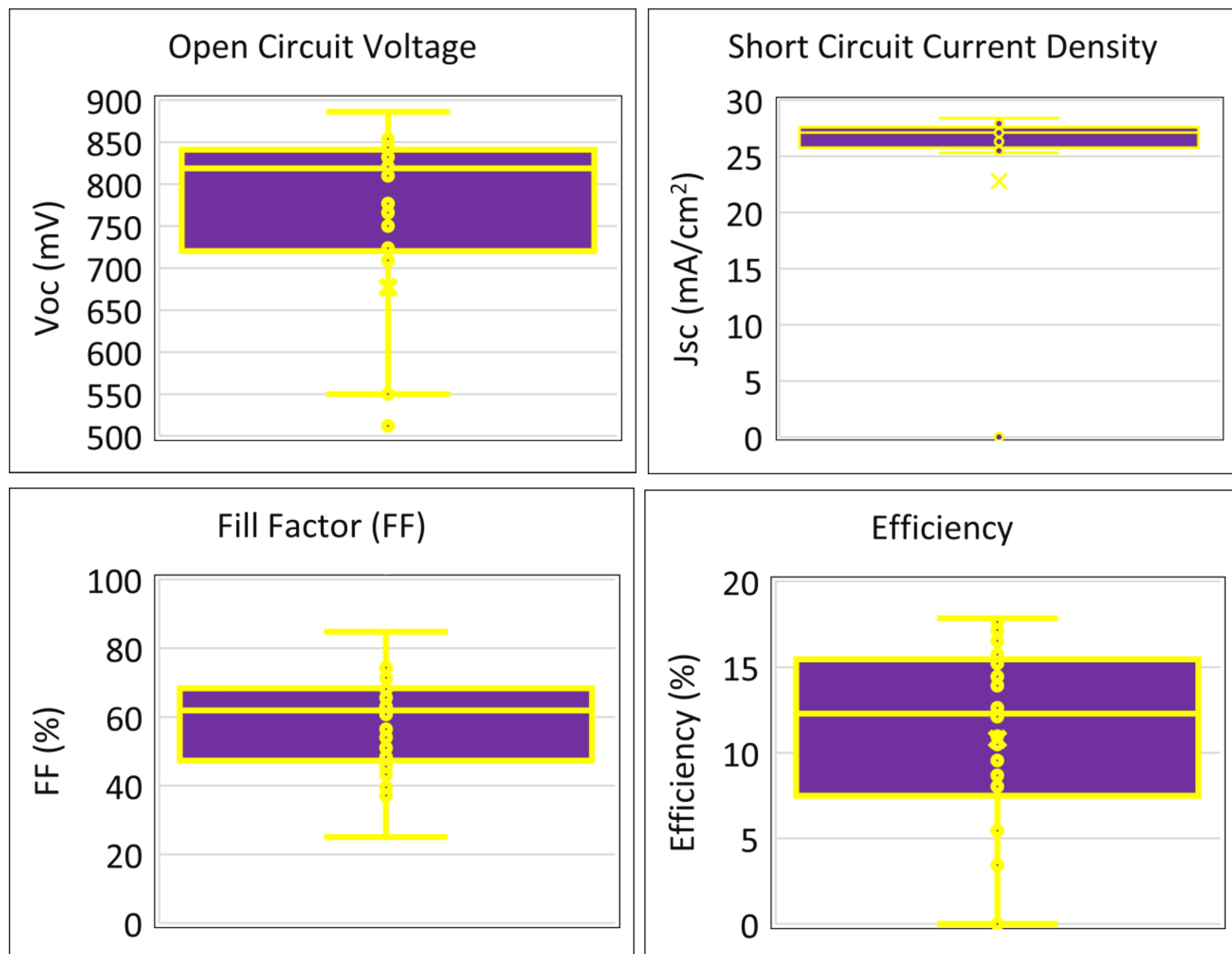

Figure 44 J-V parameters of As doped samples with TeO2 and mild Cu doping to improve current.

7.4 J-V parameters of undoped samples with TeO_2

The As doped samples without TeO_2 had extremely poor performance. However, as soon as a layer of TeO_2 was introduced by rapid oxidation, the performance improved by a factor of 3. Therefore, here the results of an undoped bilayer sample with TeO_2 are presented to isolate the effect of this metal oxide, demonstrated in Figure 45, structure can be seen in Figure 38 (e). Additionally, the J-V curve is provided in Figure 46.

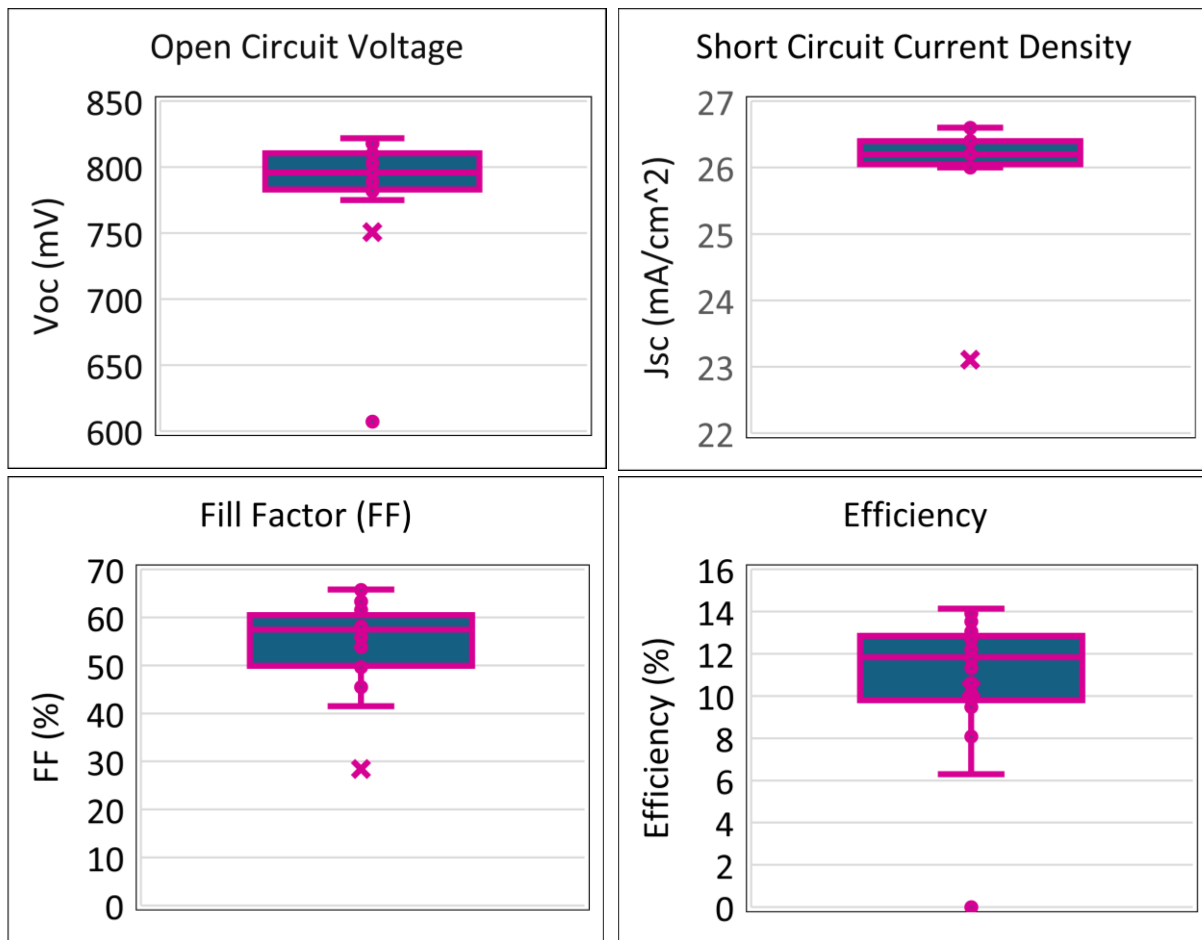

Figure 45 J-V parameters of an undoped bilayer sample with TeO2.

From the boxplots in Figure 44, the J_{sc} has an extremely tight spread and is well behaved without any intentional ohmic contact. Additionally, the V_{oc} is over 800 mV for 50% of the cells in this sample and the best performing cell has over 14% efficiency. This uptick in voltage may mean that a gradient has

been created in the bands of CdTe at the back surface. However, this would need further investigation. Now, from the J-V curve of tow of the best performing cells on this sample, a series resistance is observed. While this can be overcome with an appropriate ohmic contact, it may mean a reduction in V_{oc}.

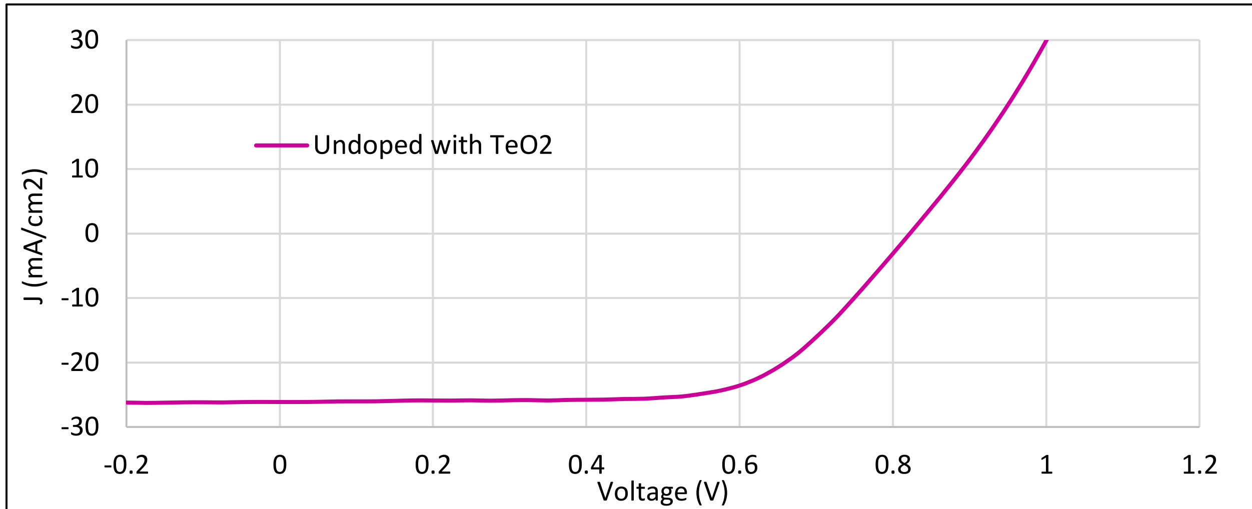

Figure 46 J-V curve of the best performing cell in the undoped bilayer sample with TeO2.

7.5 J-V parameters of CSU's baseline samples

To get a fair comparison of the results from sections 7.1 through 7.4, the results are compared with CSU's baseline Cu doped bilayer PV cells. In addition to this, a direct comparison of the undoped bilayer with TeO_2 from section 7.4 is compared with an undoped bilayer without the TeO_2 to isolate that effect as well. The electrical parameters for Cu doped bilayer samples are shown in Figure 47 and for the undoped bilayer samples, in Figure 48. The device structure is given in Figure 38 (b) & (d), respectively.

7.5.1 Cu doped bilayer samples

Overall, these cells performed better than the As dopes cells without TeO_2 and worse than the ones with TeO_2 and, with mild Cu doping (section 7.1, 7.2, and 7.3 respectively). However, the statistical spread of all data points for voltage, current density, FF, and efficiency is tight. The J_{sc} behaved as expected with Cu forming an ohmic contact for CdTe. Still, it cannot be said that As doped devices with and without TeO_2 performed better than that of Cu, since CSU's champion cell has demonstrated an

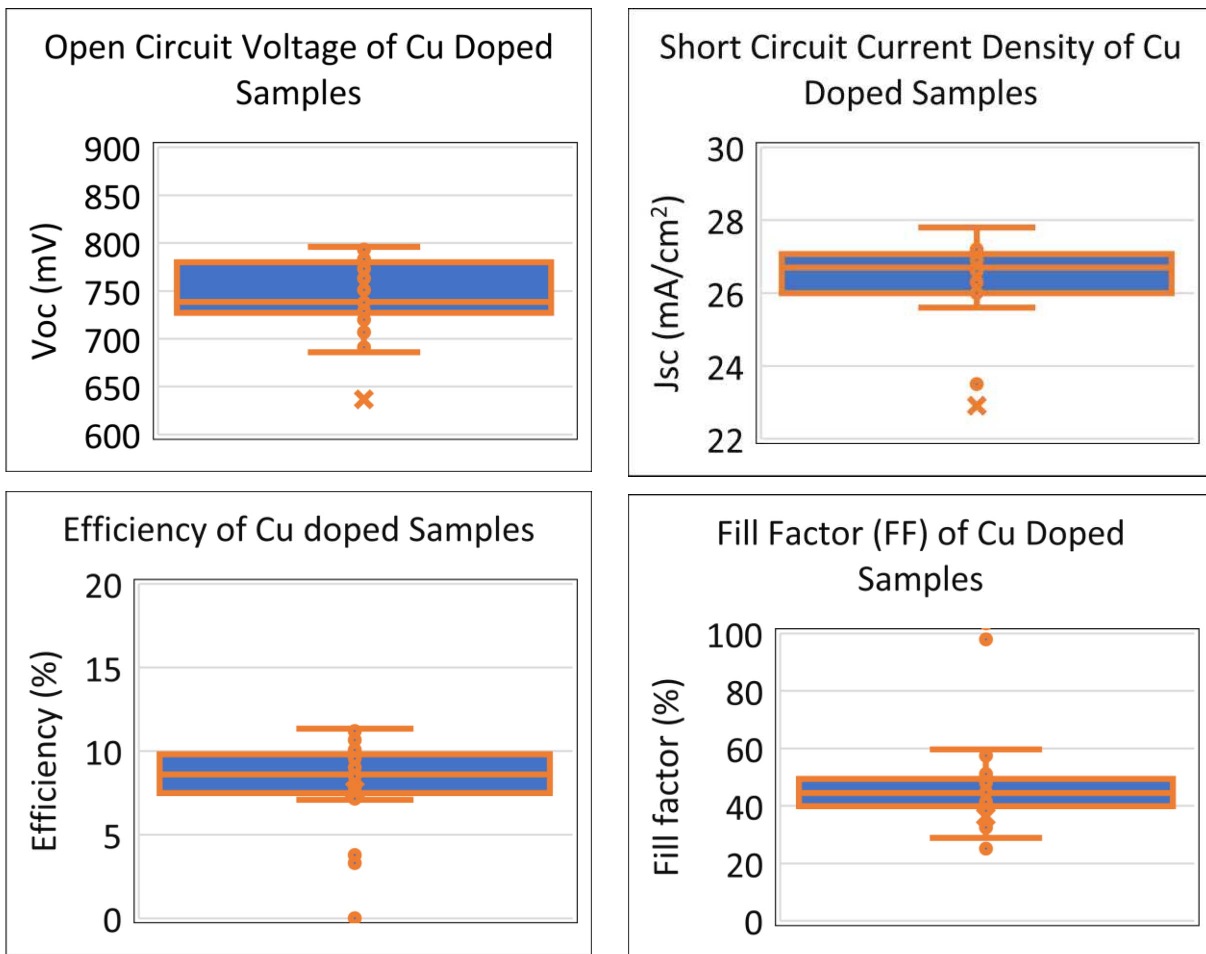

Figure 47 J-V parameters of Cu doped bilayer baseline samples.

efficiency of 20.14% [22]. The limiting factor for these Cu doped cells will need to be thoroughly investigated by characterization methods in the future.

7.5.2 Undoped bilayer samples without TeO_2

The undoped samples' cells performed worse than the ones with TeO_2 and no intentional doping (section 7.4). The efficiencies were down by 4% on average and the V_{oc} was 790 mV, 96 mV lower than the highest V_{oc} of 886 in the case of the undoped bilayer with TeO_2 by rapid oxidation. These box plots are seen in Figure 48.

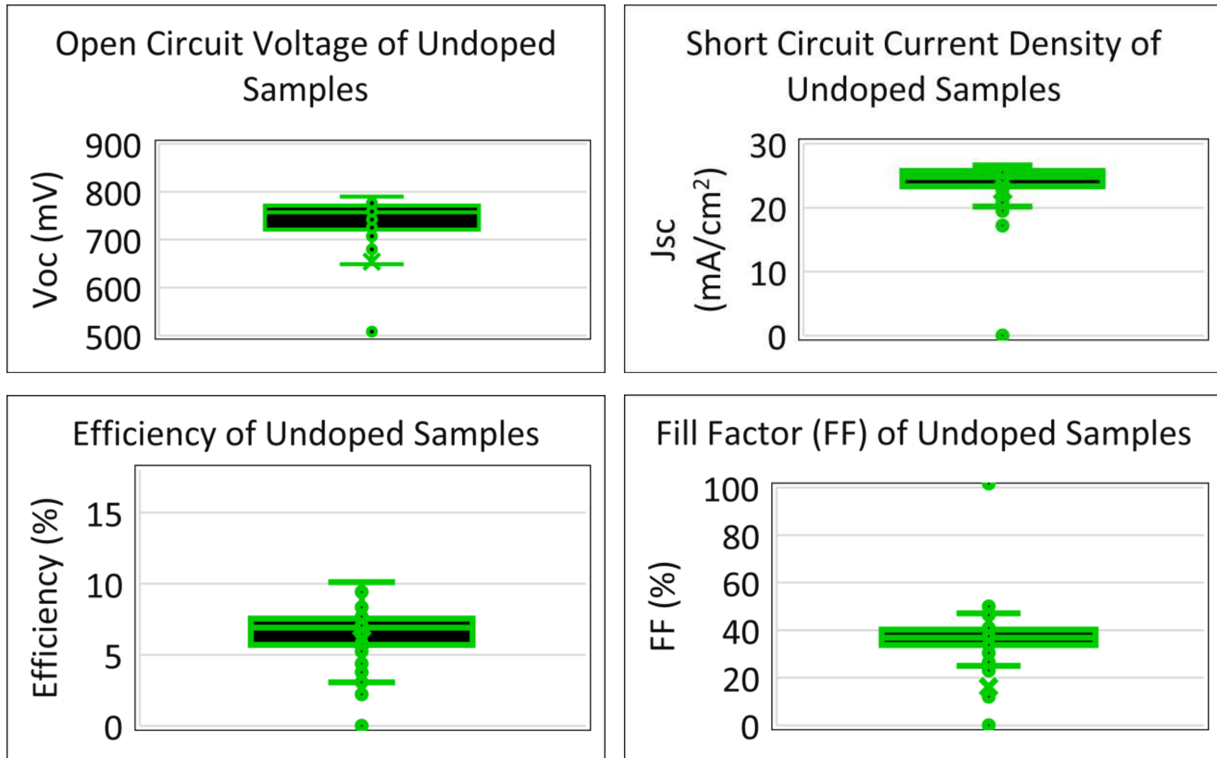

Figure 48 J-V parameters of undoped bilayer samples.

7.6 C-V Characterization

For the device structures given in Figure 38, capacitance voltage characterization was performed for the best performing cells. C-V measurements and consequently the net hole concentration as a function of depletion width were calculated by the LABVIEW VI. This information provides insight into

the carrier concentration of As doping and comparison with Cu doping of CdTe PV cells. Additionally, the effect of TeO_2, if any, is shown in the C-V profiles in Figure 49.

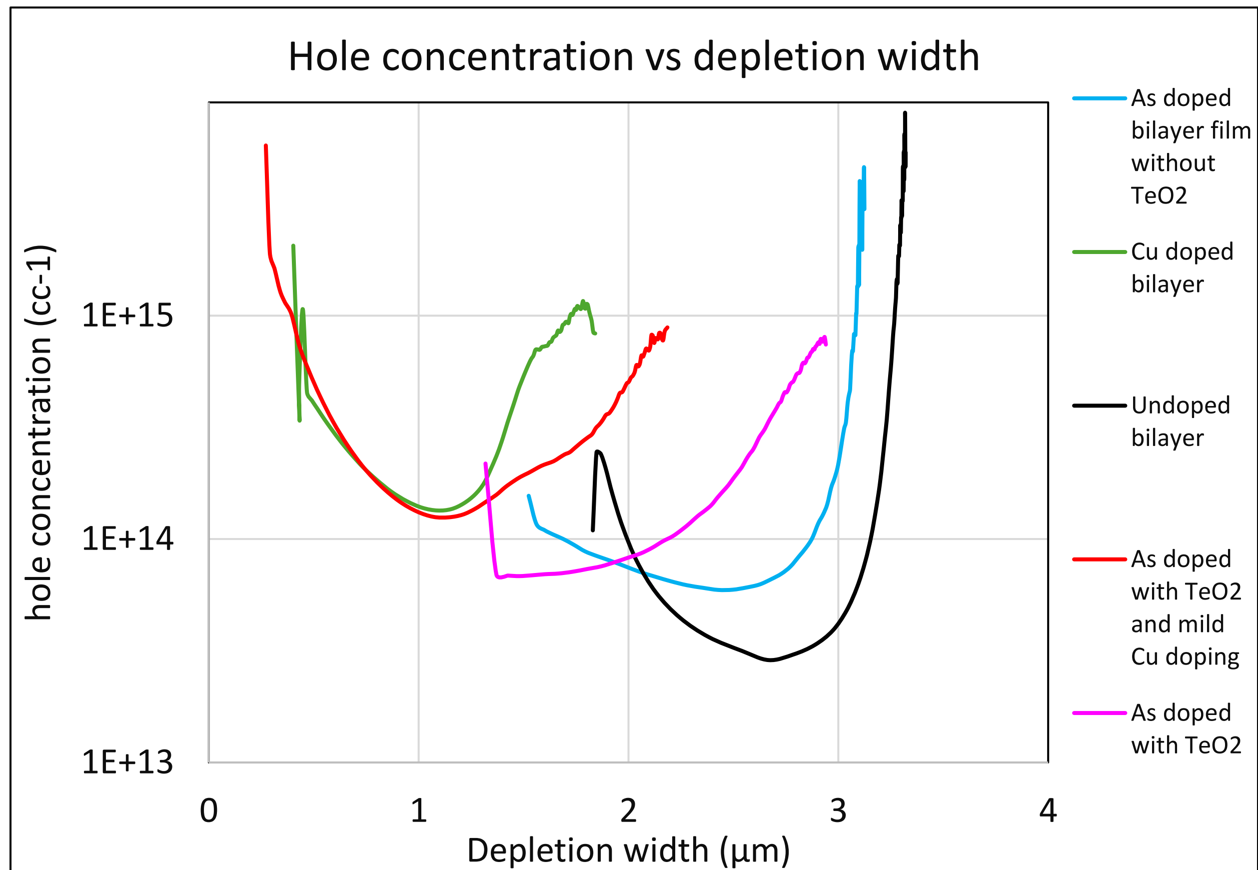

Figure 49 Net hole concentration vs depletion width of bilayer cells. Legend (right) indicates doping and surface treatment.

Assuming the concentration of As through the thickness of the films (3.5 µm) is the same as shown in the SIMS concentration profile Figure 25, the doping efficiency, or activation, which is the quotient of the hole concentration divided by the dopant concentration, is poor for the As doped samples, regardless of the presence of TeO_2. The depletion width is also unchanged, indicating this ineffective doping. However, the sample that had undergone mild Cu doping following the As doping and TeO_2 formation, shows slight improvement in the hole concentration. The baseline Cu doped cell exhibits better carrier concentration than the rest of the cells with distinct film structures. Further, the behavior of these hole concentrations is unusual, and is somewhat similar to that of a hyper-abrupt varactor diode

[47]. The hole concentration of the undoped bilayer is assumed to be the intrinsic carrier concentration of CdTe.

Previously at CSU, the Cd_3As_2 treatment for As doping was performed in the ARDS at a higher vacuum (40 mTorr), than the HBJ (1 Torr), which is the current system being used for this treatment. This implies that the content of O_2 in the ARDS is significantly lower than that of the HBJ. According to data from these previous experiments of As doping using Cd_3As_2 in the ARDS, the hole concentrations should be much higher than what are seen in Figure 49. This previously acquired data in Figure 50 shows and

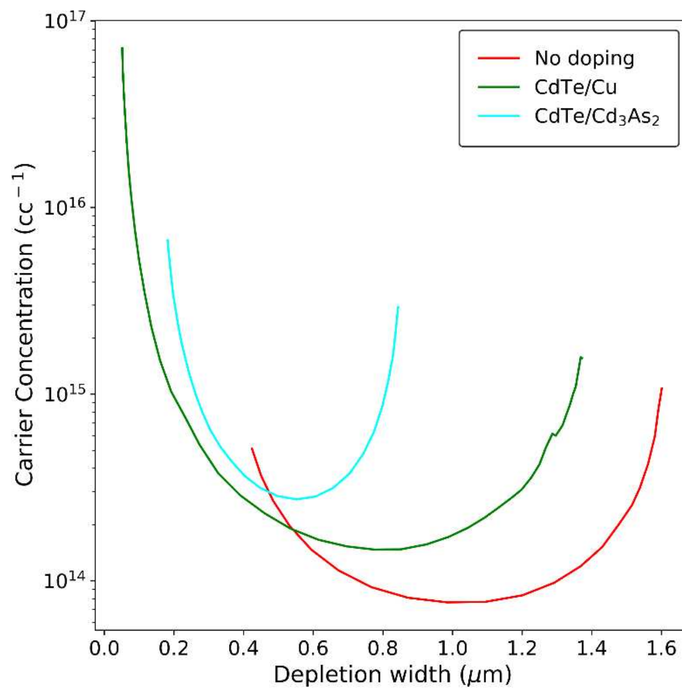

Figure 50 Net hole concentration vs depletion width of bilayer samples with As doping performed in the ARDS, Cu doping performed in the CuCl sublimation system, and an undoped cell. Data from Akash Shah.

increase in the hole concentration of As doped CdTe cell by a factor of ~2, compared to a Cu doped baseline cell. Therefore, this is further evidence that the presence of O_2 during the Cd_3As_2 treatment inhibits the activation of As, and hence, the desired device performance.

Below is a summary of the best performing parameters from several bilayer cells with varying surface treatments.

Table 1 Summary of best-performing electrical parameters of bilayer cells with various surface treatments

Structure	Electrical Parameter			
	V_{oc} (mV)	J_{sc} (mA/cm^2)	FF (%)	Efficiency (%)
Bilayer/As/TeO2	870	27.1	72.8	15.8
Bilayer/Undoped				
Bilayer/As doped	758	21.7	52.4	7.6
Bilayer/As doped/TeO_2/mild Cu doping	886	28.4	74.3	17.8
Bilayer/Undoped/TeO_2	822	26.6	65.7	14.14
Baseline bilayer Cu doped	793	27.8	60.1	11.2

Chapter 8: CONCLUSIONS AND FUTURE WORKS

8.1 Summary of results

Overall, the investigations into the three hypotheses were successful in proving or disproving these statements. Additionally, the further investigations into device characterization, kinetic behavior, doping efficiency, and surface analysis provided valuable insight into the physical, chemical, and electronic nature of CdTe thin film PV devices with distinct doping as surface treatments, such as: TeO_2 is formed quicky and natively at the back surface of CdTe by annealing the film in vacuum at high temperature and exposing it rapidly to ambient air. The TeO_2 layer survives the temperatures of the $CdCl_2$ treatment, which are an average of 400°C, indicating its stability. TeO_2 formed with this rapid oxidation greatly improves the overall photoluminescence emission and lowers the emission from the sub-bandgap defect state in $CdSe_xTe_{1-x}$. As doping does not lower this same sub-bandgap emission in $CdSe_xTe_{1-x}$, high oxygen presence during the As doping process in the HBJ by using Cd_3As_2 as the source charge inhibits dopant activation and device performance, As cannot form an effective metal-semiconductor contact with CdTe, device performance of As doped devices is vastly improved due to TeO_2 and improved further with a mild Cu doping serving as the ohmic contact.

8.2 Future works

There is a substantial difference between the devices that were doped with As using Cd_3As_2 in the ARDS, and in the HBJ. For future studies, the Cd_3As_2 treatment will be carried out in a higher vacuum system to mitigate the suspected effect of O_2, and the differences between the results from this work will be studied.

The mechanism of formation of TeO_2 by rapid oxidation of the CdTe surface needs to be thoroughly understood. Experiments involving the calculation of the enthalpy of formation of this metal

oxide need to be conducted. Further, TeO_2 exists in 3 phases [ref], α, β, and ϒ, with varying degrees of crystallinity. This atomic structure requires investigation through X-ray diffraction (XRD), or other suitable methods, to determine the interface mechanics with the CdTe lattice.

Finally, how TeO_2 mitigates the sub-bandgap emission due to the defect in $CdSe_xTe_{1-x}$ must be characterized with more advanced optical characterization tools, such as time resolved photoluminescence (TRPL), to understand this perplexing phenomenon, wherein an undoped sample with this metal oxide at the back surface can mitigate some defect deep within the bulk of the material.

References

[1] Forster, Piers M et al. “Indicators of Global Climate Change 2022: Annual Update of Large-Scale Indicators of the State of the Climate System and Human Influence.” *Earth system science data* 15.6 (2023): 2295–2327. Web.

[2] Lindsey, Rebecca, and LuAnn Dahlman. "Climate change: Global temperature." *Climate. gov* 16 (2020).

[3] Hugonnet, Romain et al. “Accelerated Global Glacier Mass Loss in the Early Twenty-First Century.” *Nature (London)* 592.7856 (2021): 726–731. Web.

[4] IEA (2024), Renewables 2023, IEA, Paris https://www.iea.org/reports/renewables-2023, Licence: CC BY 4.0

[5] Ahsan, S.M. and Khan, H.A. (2019), Performance comparison of CdTe thin film modules with c-Si modules under low irradiance. IET Renewable Power Generation, 13: 1920-1926. https://doi.org/10.1049/iet-rpg.2018.5479

[6] Amine Allouhi, Shafiqur Rehman, Mahmut Sami Buker, Zafar Said, Up-to-date literature review on Solar PV systems: Technology progress, market status and R&D, Journal of Cleaner Production, Volume 362, 2022, 132339, ISSN 0959-6526, https://doi.org/10.1016/j.jclepro.2022.132339.

[7] Encyclopædia Britannica, “Periodic Table of the Elements.” [Online]. Available: https://www.britannica.com/science/periodic-table. [Accessed: 03-Jul-2019].

[8] Gebhard, Florian, and Florian Gebhard. *Metal—insulator transitions*. Springer Berlin Heidelberg, 1997.

[9] Akash Peshin, “What are semiconductors? And how do they work?,” 2021. [Online]. Available: https://www.scienceabc.com/innovation/what-are-semiconductors-and-how-do-they-work.html.

[10] Hubbard, Seth. “PN Junctions and the Diode Equation.” *Photovoltaic Solar Energy*. Chichester, UK: John Wiley & Sons, Ltd, 2016. 54–66. Web.

[11] Munshi, Amit H., et al. "Thin-film CdTe photovoltaics–The technology for utility scale sustainable energy generation." *Solar Energy* 173 (2018): 511-516.

[12] W. Shockley and H. J. Queisser, “Detailed Balance Limit of Efficiency of p-n junction solar cells,” *J. Appl. Phys.*, vol. 32, no. 3, pp. 510–519, 1961.

[13] Scarpulla, Michael A., et al. "CdTe-based thin film photovoltaics: Recent advances, current challenges and future prospects." *Solar Energy Materials and Solar Cells* 255 (2023): 112289.

[14] F. Molva, J. P. Chamonal, and J. L. Pautrat, “Shallow Acceptors in Cadmium Telluride,” *Phys. Status Solidi*, vol. 109, no. 2, pp. 635–644, 1982, doi: 10.1002/pssb.2221090222.

[15] J. H. Yang, W. K. Metzger, and S. H. Wei, “Carrier providers or killers: The case of Cu defects in CdTe,” *Appl. Phys. Lett.*, vol. 111, no. 4, 2017, doi: 10.1063/1.4986077.

[16] E. Kučys, J. Jerhot, K. Bertulis, and V. Bariss, “Copper impurity behaviour in CdTe films,” *Phys. Status Solidi*, vol. 59, no. 1, pp. 91–99, 1980, doi: 10.1002/pssa.2210590112.

[17] D. Krasikov, A. Knizhnik, B. Potapkin, S. Selezneva, and T. Sommerer, “First-principles-based analysis of the influence of Cu on CdTe electronic properties,” *Thin Solid Films*, vol. 535, no. 1, pp. 322–325, 2013, doi: 10.1016/j.tsf.2012.10.027.

[18] L. Zhang, J. L. F. Da Silva, J. Li, Y. Yan, T. A. Gessert, and S. H. Wei, “Effect of copassivation of Cl and Cu on CdTe grain boundaries,” *Phys. Rev. Lett.*, vol. 101, no. 15, pp. 1–4, 2008, doi: 10.1103/PhysRevLett.101.155501.

[19] J. Perrenoud *et al.*, “A comprehensive picture of Cu doping in CdTe solar cells,” *J. Appl. Phys.*, vol. 114, no. 17, 2013, doi: 10.1063/1.4828484.

[20] Y. Yan, K. Jones, J. Zhou, and M. Al-Jassim, “TEM study of Locations of Cu in CdTe Solar Cells,” *MRS Proc.*, vol. 1012, 2007.

[21] E.D. Jones, N.M. Stewart, J.B. Mullin, The diffusion of copper in cadmium telluride, Journal of Crystal Growth, Volume 117, Issues 1–4, 1992, Pages 244-248, ISSN 0022-0248, https://doi.org/10.1016/0022-0248(92)90753-6.

[22] Shimpi, Tushar, et al. "Influence of Process Parameters and Absorber Thickness on Efficiency of Polycrystalline CdSeTe/CdTe Thin Film Solar Cells." *2020 47th IEEE Photovoltaic Specialists Conference (PVSC)*. IEEE, 2020.

[23] Zhao, Yuan, et al. "Monocrystalline CdTe solar cells with open-circuit voltage over 1 V and efficiency of 17%." *Nature Energy* 1.6 (2016): 1-7.

[24] J. M. Burst *et al.*, “CdTe solar cells with open-circuit voltage breaking the 1V barrier,” *Nat. Energy*, vol. 1, no. 4, 2016, doi: 10.1038/NENERGY.2016.15.

[25] S. Farrell, T. M. Barnes, W. K. Metzger, J. Park, R. Kodama, and S. Sivananthan, “In Situ Arsenic Doping of CdTe-Si by molecular beam epitaxy,” *J. Electron. Mater.*, vol. 44, no. 9, 2015.

[26] B. E. Mccandless *et al.*, “Overcoming Carrier Concentration Limits in Polycrystalline CdTe Thin Films with in situ doping,” *Sci. Rep.*, vol. 8, 2018.

[27] Danielson, Adam, et al. "Doping cdte absorber cells using group v elements." *2018 IEEE 7th World Conference on Photovoltaic Energy Conversion (WCPEC)(A Joint Conference of 45th IEEE PVSC, 28th PVSEC & 34th EU PVSEC)*. IEEE, 2018.

[28] R. Mallick et al., "Arsenic-Doped CdSeTe Solar Cells Achieve World Record 22.3% Efficiency," in IEEE Journal of Photovoltaics, vol. 13, no. 4, pp. 510-515, July 2023, doi: 10.1109/JPHOTOV.2023.3282581.

[29] Lustig, Z. F. (2022). *Improving Thin-Film Polycrystalline CdSeTe/CdTe Solar Cell Efficiencies Through Statistical Design of Experiments* (Masters Thesis, Colorado State University).

[30] Metzger, Wyatt K., et al. "Exceeding 20% efficiency with in situ group V doping in polycrystalline CdTe solar cells." *Nature Energy* 4.10 (2019): 837-845.

[31] C. Moffett, “Characterization of Tellurium back contact layer for CdTe thin film devices,” Colorado State University, 2018.

[32] Kephart, J. M., Kindvall, A., Williams, D., Kuciauskas, D., Dippo, P., Munshi, A., & Sampath, W. S. (2018). Sputter-deposited oxides for interface passivation of CdTe photovoltaics. *IEEE Journal of Photovoltaics*, *8*(2), 587-593.

[33] Danielson, A., Munshi, A., Onno, A., Weigand, W., Kindvall, A., Reich, C., ... & Sampath, W. (2019, June). Sputtered Aluminum Oxide and p+ Amorphous Silicon Back-Contact for Improved Hole Extraction in Polycrystalline CdSe x Te 1-x and CdTe Photovoltaics. In *2019 IEEE 46th Photovoltaic Specialists Conference (PVSC)* (pp. 3018-3023). IEEE.

[34] C. L. Perkins *et al.*, “Interfaces Between CdTe and ALD Al2O3,” *IEEE J. Photovoltaics*, vol. 8, no. 6, pp. 1858–1861, 2018, doi: 10.1109/jphotov.2018.2870139.

[35] Farrell, John, et al. "Characterizing TeO 2 Formation in CdTe Devices Using Transmission Electron Microscopy." *2023 IEEE 50th Photovoltaic Specialists Conference (PVSC)*. IEEE, 2023.

[36] Ponce, F. A. (1982). Imaging of interfaces in semiconductor materials using high resolution transmission electron microscopy. *Ultramicroscopy*, *9*(3), 215-219.

[37] Yi, X., & Liou, J. J. (1995). Surface oxidation of polycrystalline cadmium telluride thin films for Schottky barrier junction solar cells. *Solid-state electronics*, *38*(6), 1151-1154.

[38] J. M. Kephart, "OPTIMIZATION OF THE FRONT CONTACT TO MINIMIZE SHORTCIRCUIT CURRENT LOSSES IN CDTE THIN-FILM SOLAR CELLS," 2015.

[39] Swann, S. "Magnetron Sputtering." *Physics in technology* 19.2 (1988): 67–75. Web.

[40] D. E. Swanson et al., "Single vacuum chamber with multiple close space sublimation sources to fabricate CdTe solar cells," J. Vac. Sci. Technol. A Vacuum, Surfaces, Film., vol. 34, no. 2, p. 021202, 2016.

[41] Fred A. Stevie, Carrie L. Donley; Introduction to x-ray photoelectron spectroscopy. *J. Vac. Sci. Technol. A* 1 December 2020; 38 (6): 063204. https://doi.org/10.1116/6.0000412

[42] Lyons, V. J., and V. J. Silvestri. "Solid-Vapor Equilibria for the Compounds Cd3As2 and CdAs2." *The Journal of Physical Chemistry* 64.2 (1960): 266-269.

[43] Shewmon, Paul, ed. *Diffusion in solids*. Springer, 2016.

[44] Chu, T. L., Shirley S. Chu, and S. T. Ang. "Surface passivation and oxidation of cadmium telluride and properties of metal-oxide-CdTe structures." *Journal of applied physics* 58.8 (1985): 3206-3210.

[45] Onno, Arthur, et al. "Understanding what limits the voltage of polycrystalline CdSeTe solar cells." *Nature Energy* 7.5 (2022): 400-408.

[46] Kuciauskas, Darius, et al. "Why Increased CdSeTe Charge Carrier Lifetimes and Radiative Efficiencies did not Result in Voltage Boost for CdTe Solar Cells." *Advanced Energy Materials* 13.35 (2023): 2301784.

[47] Lundien, K., et al. "Hyperabrupt junction varactor diodes for millimeter-wavelength harmonic generators." *IEEE Transactions on Microwave Theory and Techniques* 31.2 (1983): 235-238.

APPENDIX A – PUBLICATIONS

1. Mate, Mayank, et al. "Effect of Arsenic Doping in Polycrystalline Thin Film CdTe Solar Cells." *2023 IEEE 50th Photovoltaic Specialists Conference (PVSC)*. IEEE, 2023.
2. Hill, Blake, et al. "Investigation of Sputtered P-Type Electrical Contacts for Thin Film Cadmium Telluride-Based Solar Cells." *2023 IEEE 50th Photovoltaic Specialists Conference (PVSC)*. IEEE, 2023.
3. Mate, M., Shah, A., Pandey, R., Lustig, Z., Sampath, W., & Munshi, A. H. (2024, June). Theoretical Modeling and Experimental Data of Cu and As diffusion in Thin Film CdTe Solar Cells. In 2024 IEEE 50th Photovoltaic Specialists Conference (PVSC) (pp. 1-3). IEEE.
4. Journal manuscript in progress.